PHYSICAL REVIEW D **92,** 114513 (2015)

Nucleon and pion structure with lattice QCD simulations at physical value of the pion mass

A. Abdel-Rehim,[1] C. Alexandrou,[1,2] M. Constantinou,[1,2] P. Dimopoulos,[3,4] R. Frezzotti,[4,5] K. Hadjiyiannakou,[1,2]
K. Jansen,[6] Ch. Kallidonis,[1] B. Kostrzewa,[6,7] G. Koutsou,[1] M. Mangin-Brinet,[8] M. Oehm,[9]
G. C. Rossi,[4,5] C. Urbach,[9] and U. Wenger[10]

[1]*Computation-based Science and Technology Research Center,*
The Cyprus Institute, 20 Kavafi Street, Nicosia 2121, Cyprus
[2]*Department of Physics, University of Cyprus, P.O. Box 20537, 1678 Nicosia, Cyprus*
[3]*Centro Fermi-Museo Storico della Fisica e Centro Studi e Ricerche Enrico Fermi Compendio del Viminale,*
Piazza del Viminiale 1, I-00184, Rome, Italy
[4]*Dipartimento di Fisica, Universitá di Roma Tor Vergata Via della Ricerca Scientifica 1,*
I-00133 Rome, Italy
[5]*INFN, Sezione di Tor Vergata Via della Ricerca Scientifica 1, I-00133 Rome, Italy*
[6]*NIC, DESY, Platanenallee 6, D-15738 Zeuthen, Germany*
[7]*Institut für Physik, Humboldt-Universität zu Berlin, Newtonstrasse 15, 12489 Berlin, Germany*
[8]*Theory Group, Laboratoire de Physique Subatomique et de Cosmologie, 38026 Grenoble, France*
[9]*HISKP (Theory), Bonn University, Nussallee 14-16, Bonn, Germany*
[10]*Albert Einstein Center for Fundamental Physics, University of Bern, CH-3012 Bern, Switzerland*

(Received 22 July 2015; published 31 December 2015)

We present results on the nucleon scalar, axial, and tensor charges as well as on the momentum fraction, and the helicity and transversity moments. The pion momentum fraction is also presented. The computation of these key observables is carried out using lattice QCD simulations at a physical value of the pion mass. The evaluation is based on gauge configurations generated with two degenerate sea quarks of twisted mass fermions with a clover term. We investigate excited states contributions with the nucleon quantum numbers by analyzing three sink-source time separations. We find that, for the scalar charge, excited states contribute significantly and to a less degree to the nucleon momentum fraction and helicity moment. Our result for the nucleon axial charge agrees with the experimental value. Furthermore, we predict a value of 1.027(62) in the $\overline{\mathrm{MS}}$ scheme at 2 GeV for the isovector nucleon tensor charge directly at the physical point. The pion momentum fraction is found to be $\langle x\rangle^{\pi^\pm}_{u-d} = 0.214(15)(^{+12}_{-9})$ in the $\overline{\mathrm{MS}}$ at 2 GeV.

DOI: 10.1103/PhysRevD.92.114513 PACS numbers: 11.15.Ha, 12.38.Aw, 12.38.Gc, 14.70.Dj

I. INTRODUCTION

The nucleon axial-vector coupling or nucleon axial charge g_A is experimentally a well-known quantity determined from the β-decay of the neutron. It is a key parameter for understanding the chiral structure of the nucleon and a quantity that has been studied extensively in chiral effective theories [1,2]. A description of baryon properties in chiral effective theory requires as an input g_A, and thus its value at the chiral limit and its dependence on the pion mass constitute important information that lattice QCD can provide. Its importance for phenomenology as well as the fact that it is rather straightforward to compute in lattice QCD have made it one of the most studied quantities within different fermion discretization schemes [3–9]. In lattice QCD, g_A is determined directly from the zero momentum transfer nucleon matrix element of the axial-vector current without requiring any extrapolation from finite momentum transfer calculations as, for example, is required for the anomalous magnetic moment of the nucleon. In addition, being an isovector quantity, it does not receive any contributions from the coupling of the current to closed quark loops, and thus one only needs to compute the connected contribution with well-established lattice QCD techniques. Therefore, g_A has come to be regarded as a prime benchmark quantity for the computation of lattice QCD matrix elements. Postdiction of the value of g_A within lattice QCD is, therefore, regarded as an essential step before the reliable prediction of other couplings and form factors for which the same formalism is used.

Unlike g_A, the nucleon scalar and tensor charges are not well known. Limits on the value of the scalar and tensor coupling constants arise from $0^+ \to 0^+$ nuclear decays and the radiative pion decay $\pi \to e\nu\gamma$, respectively. They have become the focus of planned experiments to search for physics beyond the familiar weak interactions of the Standard Model sought in the decay of ultracold neutrons [10]. The computation of the tensor charge is particularly timely since new experiments using polarized ^{3}He/Proton at Jefferson lab aim at increasing the experimental accuracy of its measurement by an order of magnitude [11]. In addition, experiments at the LHC are expected to increase the limits to contributions arising from tensor and scalar interactions by an order of magnitude making these observables interesting probes of new physics originating at the TeV scale. Computing the scalar charge will also provide input for dark matter searches. Experiments, which aim at a direct detection of dark matter, are based on measuring the recoil energy of a nucleon hit by a dark matter candidate. In many supersymmetric scenarios [12] and in some Kaluza-Klein extensions of the standard model [13,14], the dark matter nucleon interaction is mediated through a Higgs boson. In such a case, the theoretical expression of the spin-independent scattering amplitude at zero momentum transfer involves the quark content of the nucleon or the nucleon sigma-term, which is closely related to the scalar charge. In fact, this contributes the largest uncertainty on the nucleon dark matter cross section. Therefore, computing the scalar g_S and tensor g_T charges of the nucleon within lattice QCD will provide useful input for the ongoing experimental searches for beyond the standard model physics.

Another experimental frontier that provides information on the quark and gluon structure of a hadron, is the measurement of parton distribution functions (PDFs) in a variety of high energy processes such as deep-inelastic lepton scattering and Drell-Yan in hadron-hadron collisions. PDFs give, to leading twist, the probability of finding a specific parton in the hadron carrying certain momentum and spin, in the infinite momentum frame. Their universal nature relies on factorization theorems that allow differential cross sections to be written in terms of a convolution of certain process-dependent coefficients that encode the hard perturbative physics and process-independent PDFs that describe the soft, nonperturbative physics at a factorization energy scale μ [15,16]. Because these PDFs are light-cone correlation functions, it is not straightforward to calculate them directly in Euclidean space. Instead, one calculates Mellin moments of the PDFs expressed in terms of hadron matrix elements of local operators, which through the operator product expansion are related to the original light-cone correlation functions. Mellin moments are measured or extracted from phenomenological analyses in deep-inelastic scattering experiments, and thus they can be directly compared to lattice results when converted to the same energy scale μ.

In this work, we consider the three first moments that one can construct, namely, the first moment of the spin-independent (or unpolarized) $q = q_\downarrow + q_\uparrow$, helicity (or polarized) $\Delta q = q_\downarrow - q_\uparrow$, and transversity $\delta q = q_\top + q_\perp$ distributions, which are defined as follows:

$$\langle x \rangle_q = \int_0^1 x[q(x) + \bar{q}(x)]dx \tag{1}$$

$$\langle x \rangle_{\Delta q} = \int_0^1 x[\Delta q(x) - \Delta\bar{q}(x)]dx \tag{2}$$

$$\langle x \rangle_{\delta q} = \int_0^1 x[\delta q(x) + \delta\bar{q}(x)]dx, \tag{3}$$

where $q_\downarrow$ and $q_\uparrow$ correspond, respectively, to quarks with helicity aligned and antialigned with that of a longitudinally polarized target and $q_\top$ and $q_\perp$ correspond to quarks with spin aligned and antialigned with that of a transversely polarized target. These moments, at leading twist, can be extracted from the hadron matrix elements of one-derivative vector, axial-vector, and tensor operators at zero momentum transfer. Thus, they constitute the next level of observables in terms of complexity that can be computed in lattice QCD after the coupling constants that do not involve derivative operators. The unpolarized and polarized moments $\langle x \rangle_q$ and $\langle x \rangle_{\Delta q}$ of the nucleon are measured experimentally, and thus lattice QCD provides a postdiction, while a computation of the nucleon transversity $\langle x \rangle_{\delta q}$ provides a prediction. It is worth mentioning a new approach proposed recently for measuring directly the PDFs within lattice QCD [17,18], which is currently under investigation [19,20].

In this paper, we extend the analysis of meson masses, the muon anomalous magnetic moment $g-2$, and the meson decay constants considered in Ref. [21], to the nucleon matrix elements for the three first Mellin moments, while for the pion we compute the momentum fraction. While the present paper builds on the methodology developed in Refs. [22–26], this work presents the first evaluation of these six quantities directly at the physical value of the pion mass. This is a substantial step forward since it avoids chiral extrapolations, which are often difficult and can lead to rather large systematic uncertainties.

The paper is organized as follows. In Sec. II we define the nucleon and pion matrix elements, in Sec. III we explain the lattice methodology, in Sec. IV we give the simulation details, and in Sec. V we give our results. Section VI summarizes our findings and gives our conclusions.

II. MATRIX ELEMENTS

A. Nucleon

We are interested in extracting the forward nucleon matrix elements $\langle N(p)|\mathcal{O}|N(p)\rangle$, with p the nucleon initial and final momentum. We consider the complete set of local and one-derivative operators, yielding a nonzero result. The local scalar, axial-vector, and tensor operators are

$$\mathcal{O}_{S^a} = \bar{q}\frac{\tau^a}{2}q, \qquad \mathcal{O}^{\mu}_{A^a} = \bar{q}\gamma_5\gamma^\mu\frac{\tau^a}{2}q,$$
$$\mathcal{O}^{\mu\nu}_{T^a} = \bar{q}\sigma^{\mu\nu}\frac{\tau^a}{2}q. \tag{4}$$

We do not consider the vector operator $\overline{\psi}(x)\gamma_m u\psi(x)$ since this yields the renormalization constant Z_V, which we calculate separately using our RI-MOM setup, as explained in Sec. V. If one instead uses the lattice conserved Noether current, which we typically do in in our computation of the nucleon electromagnetic form factors, the forward matrix element trivially yields the electric charge.

The one-derivative vector, axial-vector, and tensor operators are given by

$$\begin{aligned}\mathcal{O}^{\mu\nu}_{V^a} &= \bar{q}\gamma^{\{\mu}\overleftrightarrow{D}^{\nu\}}\frac{\tau^a}{2}q,\\ \mathcal{O}^{\mu\nu}_{A^a} &= \bar{q}\gamma^{\{\mu}\overleftrightarrow{D}^{\nu\}}\gamma_5\frac{\tau^a}{2}q,\\ \mathcal{O}^{\mu\nu\rho}_{T^a} &= \bar{q}\sigma^{[\mu\{\nu]}\overleftrightarrow{D}^{\rho\}}\frac{\tau^a}{2}q,\end{aligned} \tag{5}$$

where $\bar{q} = (\bar{u}, \bar{d})$,

$$\overleftrightarrow{D}_\mu = \frac{1}{2}(\overrightarrow{D}_\mu - \overleftarrow{D}_\mu), \qquad D_\mu = \frac{1}{2}(\nabla_\mu + \nabla^*_\mu),$$

and ∇_μ (∇^*_μ) is the usual forward (backward) derivative on the lattice. The curly (square) brackets represent a symmetrization (antisymmetrization) over pairs of indices, with the symmetrization accompanied by subtraction of the trace.

In what follows, all expressions will be given in Euclidean time. For example, the one-derivative vector current that will be used in the computations of both nucleon and pion momentum fractions, in Euclidean time and setting $\mu = \nu = 4$, is given by

$$\mathcal{O}^{44}_{V^a} = \bar{q}\frac{3}{4}\left[\gamma^4\overleftrightarrow{D}^4 - \frac{1}{3}\sum_{k=1}^{3}\gamma^k\overleftrightarrow{D}^k\right]\frac{\tau^a}{2}q. \tag{6}$$

In this work, we consider the isovector quantities obtained from Eqs. (4) and (5) by using the Pauli matrix τ^3. We also consider the isoscalar combination obtained by replacing τ^a by unity. The individual up- and down-quark combinations can be extracted form the isovector and isoscalar quantities which are equivalent to replacing τ^a with the projectors onto the up- or down-quarks. The isoscalar combination and the up- and down-quark contributions receive disconnected contributions. Our high-statistics study using an $N_f = 2 + 1 + 1$ ensemble of twisted mass fermions with a pion mass of 373 MeV has shown that the disconnected contributions for the tensor isoscalar charge and the isoscalar first moments are very small compared to the connected [27,28]. In the same study, the disconnected contributions to the isoscalar axial and scalar charge were found to be about (7%–10%) of the connected. In this work, we will only compute the connected contributions. The disconnected contributions will need at least an order of magnitude more statistics and will be presented in a follow-up publication.

For zero momentum transfer, the nucleon matrix elements of the local operators in Eq. (4) can be decomposed in the following form factors:

$$\langle N(p,s')|\mathcal{O}_S|N(p,s)\rangle = \bar{u}_N(p,s')\left[\frac{1}{2}G_S(0)\right]u_N(p,s), \tag{7}$$

$$\langle N(p,s')|\mathcal{O}^\mu_A|N(p,s)\rangle = i\bar{u}_N(p,s')\left[\frac{1}{2}G_A(0)\gamma^\mu\gamma_5\right]u_N(p,s), \tag{8}$$

$$\langle N(p,s')|\mathcal{O}^{\mu\nu}_T|N(p,s)\rangle = \bar{u}_N(p,s')\left[\frac{1}{2}A_{T10}(0)\sigma^{\mu\nu}\right]u_N(p,s). \tag{9}$$

Thus, the scalar matrix element at zero momentum transfer yields the form factor $G_S(0) \equiv g_S$, the local axial-vector $G_A(0) \equiv g_A$, and the local tensor matrix element yields $A_{T10}(0) \equiv g_T$. In all these quantities, the operators are either the isovector or isoscalar combinations or individual up- or down-quark contributions. At nonzero momentum, additional form factors arise in the decomposition of Eqs. (8) and (9). Namely, the induced pseudoscalar $G_p(Q^2)$ appears as the second form factor in the decomposition of the matrix element of the axial-vector, and the form factors $B_{T10}(Q^2)$ and $\tilde{A}_{T10}(Q^2)$ appear in the decomposition of the nucleon matrix element of the tensor operator, where Q^2 is the momentum transfer square in Euclidean time. These cannot be extracted at zero momentum transfer and will not be considered in this work.

The corresponding decomposition for the one-derivative operators in Eq. (5) is given by

$$\langle N(p,s')|\mathcal{O}^{\mu\nu}_V|N(p,s)\rangle = \bar{u}_N(p,s')\left[\frac{1}{2}A_{20}(0)\gamma^{\{\mu}p^{\nu\}}\right]u_N(p,s), \tag{10}$$

$$\langle N(p,s')|\mathcal{O}^{\mu\nu}_A|N(p,s)\rangle = i\bar{u}_N(p,s')\left[\frac{1}{2}\tilde{A}_{20}(0)\gamma^{\{\mu}p^{\nu\}}\gamma^5\right]u_N(p,s), \tag{11}$$

$$\langle N(p,s')|\mathcal{O}^{\mu\nu\rho}_T|N(p,s)\rangle = i\bar{u}_N(p,s')\left[\frac{1}{2}A_{T20}(0)\sigma^{[\mu\{\nu]}p^{\rho\}}\right]u_N(p,s). \tag{12}$$

The momentum fraction, helicity moment, and the transversity moment are obtained from the above forward matrix elements by $\langle x\rangle_q = A^q_{20}(0)$, $\langle x\rangle_{\Delta q} = \tilde{A}^q_{20}(0)$, and $\langle x\rangle_{\delta q} = A^q_{T20}(0)$, respectively. Here we use the generic symbol q to denote the quark combination, where $q = u + d$ will denote the isoscalar combination, $q = u - d$ will denote the isovector combination, and $q = u$ or $q = d$ denotes the individual up- and down-quark contributions. For instance, the isovector helicity moment will be denoted as $\langle x\rangle_{\Delta u - \Delta d} = \tilde{A}^{u-d}_{20}(0)$. For uniformity in our notation, we will also write g^{u-d}_A for the nucleon axial charge, despite the fact that the measured axial charge is understood to be an isovector quantity.

B. Pion

The isovector momentum fraction of the pion $\langle x\rangle_{u-d}^{\pi^\pm}$ can be extracted from the corresponding pion matrix element of the one-derivative vector operator. Specifically, we use the following operator, sometimes also denoted as $\mathcal{O}_{v2b}$,

$$\mathcal{O}^{44}(x) = \frac{2}{3}\mathcal{O}^{44}_{V^3}(x) \tag{13}$$

where $\mathcal{O}^{44}_{V^3}(x)$ is given in Eq. (6). As in the case of the nucleon, no external momentum is needed in our calculation, which is advantageous since an external momentum increases the noise to signal ratio.

III. LATTICE METHODOLOGY

A. Correlation functions

In order to compute hadron matrix elements, we need to calculate the appropriate three-point function. We first present the setup for the nucleon matrix elements for the special case $\mathbf{q} = \mathbf{0}$. The three-point function is then given by

$$\begin{aligned} &G_{\mathrm{3pt}}^{\mu_1,\ldots,\mu_n}(\Gamma^\nu, \mathbf{p}, t_s, t_{\mathrm{ins}}) \\ &\quad = \sum_{\mathbf{x}_s,\mathbf{x}_{\mathrm{ins}}} e^{-i(\mathbf{x}_s-\mathbf{x}_0)\cdot\mathbf{p}}\Gamma^\nu_{\beta\alpha}\langle J_\alpha(\mathbf{x}_s,t_s)\mathcal{O}_\Gamma^{\mu_1,\ldots,\mu_n}(\mathbf{x}_{\mathrm{ins}},t_{\mathrm{ins}}) \\ &\qquad \times \bar{J}_\beta(\mathbf{x}_0,t_0)\rangle, \end{aligned} \tag{14}$$

where x_0, x_{ins}, and x_s are the source, insertion, and sink coordinates, respectively. In order to cancel unknown overlaps of the interpolating field with the nucleon state as well as the time evolution in Euclidean time, we construct ratios of the three-point function with the two-point function, which is given by

$$G_{\mathrm{2pt}}(\mathbf{0}, t_s) = \sum_{\mathbf{x}_s}\Gamma^4_{\beta\alpha}\langle J_\alpha(\mathbf{x}_s,t_s)\bar{J}_\beta(\mathbf{x}_0,t_0)\rangle. \tag{15}$$

The projection matrices are

$$\Gamma^4 = \frac{1}{4}(\mathbb{1}+\gamma_4), \qquad \Gamma^k = \Gamma^4 i\gamma_5\gamma_k. \tag{16}$$

We use the proton interpolating operators

$$J_\alpha(x) = \epsilon^{abc}u^a_\alpha(x)[u^{\top b}(x)C\gamma_5 d^c(x)] \tag{17}$$

with a, b, and c denoting color components. We employ Gaussian smeared quark fields [29,30] to increase the overlap with the proton state and decrease overlap with excited states. The smeared interpolating fields are given by

$$\begin{aligned} q^a_{\mathrm{smear}}(t,\mathbf{x}) &= \sum_{\mathbf{y}} F^{ab}(\mathbf{x},\mathbf{y};U(t))q^b(t,\mathbf{y}), \\ F &= (\mathbb{1}+a_G H)^{N_G}, \\ H(\mathbf{x},\mathbf{y};U(t)) &= \sum_{i=1}^{3}[U_i(x)\delta_{x,y-\hat{\imath}} + U_i^\dagger(x-\hat{\imath})\delta_{x,y+\hat{\imath}}]. \end{aligned} \tag{18}$$

We apply APE-smearing to the gauge fields U_μ entering the hopping matrix H. The parameters for the Gaussian smearing a_G and N_G are optimized using the nucleon ground state [31] such as to give a root mean square radius of about 0.5 fm. We use $(N_G, a_G) = (50, 4)$ and $(N_{\mathrm{APE}}, a_{\mathrm{APE}}) = (50, 0.5)$.

For the case of isovector quantities, the so-called disconnected contributions arising from the coupling of the operators to a sea quark shown schematically in the lower panel of Fig. 1 are zero in the isospin limit up to lattice cutoff effects. Since we work with an automatic $\mathcal{O}(a)$-improved action, we expect cutoff effects to be small for our action and lattice spacing. Thus, these correlators can be calculated by evaluating the connected diagram of Fig. 1 (upper panel) for which we employ sequential inversions through the sink [32]. For the case of isoscalar quantities, the disconnected diagrams do not vanish and need to be computed. The calculation of disconnected contributions needs special techniques and at least an order of magnitude

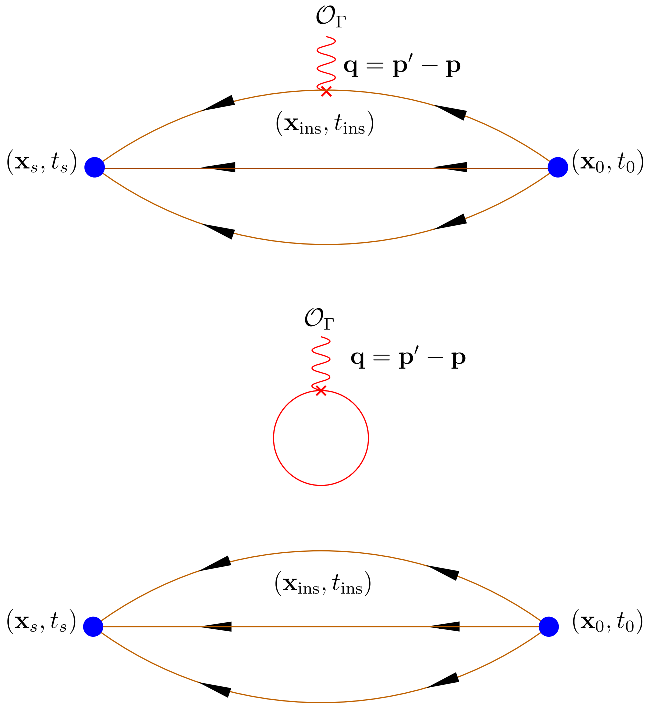

FIG. 1 (color online). Connected (upper) and disconnected (lower) contributions to nucleon three-point functions.

more statistics than the connected ones [28]. In a high-statistics analysis using $N_f = 2+1+1$ twisted mass fermions at pion mass of 373 MeV, we found that they contribute about 7% to the isoscalar axial charge, while they are negligible for the tensor charge, $\langle x\rangle_q$ and $\langle x\rangle_{\Delta q}$ [27]. In this work, we restrict ourselves to the calculation of the connected contributions.

For evaluation of the connected contribution, we take the nucleon creation operator at a position $x_0 = (\mathbf{x}_0, t_0)$, referred to as the source position, which is randomized over gauge configurations to reduce autocorrelations, and the annihilation operator at a later time t_s, the sink position x_s. The current couples to a quark at an intermediate time t_{ins}, the insertion time. In this calculation, we fix the sink and source to momentum $\mathbf{p} = \mathbf{0}$, and thus the current carries zero momentum. We employ the sequential inversion method through the sink requiring one set of sequential inversions per choice of the sink time slice t_s and sink projector. Thus, within this approach, at a fixed sink-source time separation, we obtain results for all insertion times as well as for any operator $\mathcal{O}_\Gamma^{\{\mu_1\cdots\mu_n\}}$. We perform separate inversions for the four projection matrices Γ^4 and Γ^k given in Eq. (16).

Using the two- and three-point functions of Eqs. (14) and (15), we form the ratio

$$R(\Gamma^\lambda, t_s, t_{\mathrm{ins}}) = \frac{G_{3\mathrm{pt}}(\Gamma^\lambda, \mathbf{0}, t_s, t_{\mathrm{ins}})}{G_{2\mathrm{pt}}(\mathbf{0}, t_s)} \tag{19}$$

where all time separations are given relative to the source time t_0. For large time separations, the two-point function in the denominator cancels unknown overlaps of the nucleon interpolating operators with the nucleon spinors as well as the Euclidean time evolution, such that the desired matrix element is isolated. However, in order to identify when the large time limit sets in, one has to carefully study the time dependence of the ratio since excited states contamination can affect the value of the ratio. For arbitrary times, the contributions from excited states in the ratio are

$$R(\Gamma^\lambda, t_s, t_{\mathrm{ins}}) \propto \frac{\sum_{n',n}\langle J|n'\rangle\langle n|\bar{J}\rangle\langle n'|\mathcal{O}_\Gamma|n\rangle e^{-E_{n'}(t_s-t_{\mathrm{ins}})}e^{-E_n(t_{\mathrm{ins}}-t_0)}}{\sum_n|\langle J|n\rangle|^2 e^{-E_n(t_s-t_0)}}, \tag{20}$$

where $|n\rangle$ is the nth eigenstate of the QCD Hamiltonian with the quantum numbers of the nucleon and E_n is the energy of the state in the rest frame of the nucleon. Denoting with $|0\rangle = |N\rangle$ the nucleon ground state, with $|1\rangle = |N'\rangle$ and $|2\rangle = |N''\rangle$ the first and second excited states, and with $\Delta = E_{N'} - m_N$ and $\Delta' = E_{N''} - E_{N'}$ their respective energy gaps, the ratio in Eq. (20) yields

$$R(\Gamma^\lambda, t_s, t_{\mathrm{ins}}) \propto \frac{\mathcal{M} + \mathcal{R}e^{-\Delta(t_s-t_{\mathrm{ins}})} + \mathcal{R}^\dagger e^{-\Delta(t_{\mathrm{ins}}-t_0)} + O(e^{-\Delta'(t_{\mathrm{ins}}-t_0)})}{1 + |\mathcal{C}|^2 e^{-\Delta(t_s-t_0)} + O(e^{-\Delta'(t_s-t_0)})}, \tag{21}$$

where $\mathcal{M} = \langle N|\mathcal{O}_\Gamma|N\rangle$ is the desired matrix element, $\mathcal{C} = \frac{\langle J|N'\rangle}{\langle J|N\rangle}$, and $\mathcal{R} = \mathcal{C}\langle N'|\mathcal{O}_\Gamma|N\rangle$. If the exponential terms are small compared to $\mathcal{M}$ and to unity, then we have what is referred to as ground-state dominance, and the ratio yields the desired ground state matrix element.

The computation of the pion momentum fraction is carried out along the same lines as for the nucleon. To extract the desired matrix element $\langle\pi(\mathbf{0})|\mathcal{O}^{44}|\pi(\mathbf{0})\rangle$, we construct the ratio of the appropriate three-point function with the pion two-point function with a source at t_0 and a sink at t_s:

$$R^\pi(t_s, t_{\mathrm{ins}}) = \frac{G_{3\mathrm{pt}}^{44}(\mathbf{0}, t_s, t_{\mathrm{ins}})}{G_{2\mathrm{pt}}^{\pi}(t_s)} \tag{22}$$

with

$$G_{3\mathrm{pt}}^{44}(\mathbf{0}, t_s, t_{\mathrm{ins}}) = \sum_{\mathbf{y}}\langle J_{\pi^\pm}(t_s)\mathcal{O}^{44}(t_{\mathrm{ins}}, \mathbf{y})J_{\pi^\pm}^\dagger(t_0)\rangle, \tag{23}$$

with $J_{\pi^+}(x) = \bar{d}(x)\gamma_5 u(x)$ $(J_{\pi^-}(x) = \bar{u}(x)\gamma_5 d(x))$ as the interpolating field of π^+ (π^-). As in the case of the nucleon, in the isovector combination up to lattice artifacts, the disconnected contributions vanish and will thus be dropped.

The pion two- and three-point correlators, unlike those of the nucleon, are evaluated by using a stochastic time-slice source [Z(2)-noise in both real and imaginary parts] [33–35] for all color, spin, and spatial indices. This method, which is particularly suited for the pion, was first applied to moments of parton distribution functions in Ref. [36]. The quark propagator $S_\beta^b(y)$ is obtained by solving

$$\sum_y D_{\alpha\beta}^{ab}(z, y)S_\beta^b(y) = \xi(\mathbf{z})_\alpha^a\delta_{z_0,t_0} \quad (\text{source at } t_0) \tag{24}$$

for S. $\xi(\mathbf{z})_\alpha^a$ is a $Z(2)$ random source satisfying

$$\langle\xi^*(\mathbf{x})_\alpha^a\xi(\mathbf{y})_\beta^b\rangle_r = \delta_{\mathbf{xy}}\delta_{ab}\delta_{\alpha\beta}, \langle\xi(\mathbf{x})_\alpha^a\xi(\mathbf{y})_\beta^b\rangle_r = 0, \tag{25}$$

where $\langle\cdot\rangle_r$ denotes the average over many random sources. Using S, we can define a so-called sequential or generalized propagator $\Sigma_\beta^b(y)$ from [37]

$$\sum_y D_{\alpha\beta}^{ab}(z, y)\Sigma_\beta^b(y) = \gamma_5 S_\alpha^a(z)\delta_{z_0,t_s} \quad (\text{sink at } t_s). \tag{26}$$

This method represents a generalization of the one-end-trick [38] to moments of parton distribution functions. Its clear advantage is an increased signal to noise ratio at reduced computational costs at least when it is applied for meson observables. With a point source, 24 inversions per gauge configuration are needed: 12 (3 colors × 4 spins) for the quark propagator and 12 for the generalized propagator. With the stochastic source discussed above, only two inversions are needed: one for the quark propagator and another one for the generalized propagator. For a comparison of stochastic vs point sources, we refer to Ref. [36].

The stochastic method described above can be adapted to work for other mesons. However, for moments of nucleon parton distribution functions, we found no improvement in the signal to noise ratio for a comparable computational effort.

For $\langle x\rangle^{\pi^\pm}_{u-d}$ it is sufficient to fix $t_s - t_0 = T/2$, where T is the temporal extent of the lattice. As in the case of the nucleon, the value of t_0 is chosen randomly on every gauge configuration in order to reduce autocorrelation.

B. Ensuring ground state dominance

To extract the nucleon matrix element from the ratio defined in Eq. (19), one needs to make sure that the contribution of the terms due to the excited states in the numerator and denominator of Eq. (21), the so-called contamination due to excited states, is negligible. We will employ three methods to check for ground state dominance, as described below.

In the first method, which we will refer to as the *plateau method*, one probes the region for which $\Delta(t_s - t_{\rm ins}) \gg 1$ and $\Delta(t_{\rm ins} - t_0) \gg 1$ such that excited state contributions are much smaller than the contribution of the ground state. Within this time interval, the ratio becomes time independent, and the time range where this happens is referred to as the *plateau region*. Fitting the ratio

$$R(\Gamma^\lambda, t_s, t_{\rm ins}) \xrightarrow[\Delta(t_s-t_{\rm ins})\gg 1]{\Delta(t_{\rm ins}-t_0)\gg 1} \Pi(\Gamma^\lambda) \tag{27}$$

over $t_{\rm ins}$ within this plateau region, one obtains the plateau value, which is the desired matrix element $\mathcal{M}$. To ensure excited state suppression, one repeats this procedure for multiple values of t_s, checking that the plateau value does not change. However, the statistical errors grow exponentially with t_s, which means that as the sink-source time separation increases the signal is lost as compared to the statistical noise making it difficult to detect any time dependence. Increasing t_s therefore requires a corresponding increase in statistics if this check is to be useful [25].

The second approach is to use the *summation method* proposed some time ago [39] and recently applied to the study of the nucleon axial charge [40]. One sums the ratio over the time of the insertion,

$$R^{\rm sum}(\Gamma^\lambda) = \sum_{t_{\rm ins}=t_0+\tau}^{t_s-\tau} R(\Gamma^\lambda, t_s, t_{\rm ins}), \tag{28}$$

with τ selected such that contact terms are not included, i.e., $\tau = 1$ for local operators and $\tau = 2$ for derivative operators. The sum over the excited state contributions given in Eq. (21) is a geometric series and can easily be summed to yield

$$R^{\rm sum}(\Gamma^\lambda) \propto \mathcal{C}' + (t_s - t_0)\mathcal{M} + O(e^{-\Delta(t_s-t_0)}) \tag{29}$$

with $\mathcal{C}'$ a constant independent of t_s. The advantage over the plateau method is that excited state contamination is suppressed by a larger factor $[\Delta(t_s - t_0)$ as opposed to $\Delta(t_s - t_{\rm ins})$ or $\Delta(t_{\rm ins} - t_0)]$. However, the extraction of $\mathcal{M}$ requires a fit to two parameters, resulting in general in larger statistical uncertainties. Nevertheless, this method provides a good consistency check of our results.

A third approach to extract the desired matrix element is to take into account in the fit the contribution of the first excited state in Eq. (21). In this case, we simultaneously fit the two- and three-point correlation functions obtained from the lattice including the ground state and the first excited state contributions. This is done by performing a combined fit to all sink-source separations and to both correlation functions with $t_{\rm ins}$ and t_s as independent variables. Like for the summation method, we exclude the contact terms, i.e., for $t_{\rm ins} \in [t_0 + 1, t_s - 1]$ for the scalar, axial, and tensor charges and $t_{\rm ins} \in [t_0 + 2, t_s - 2]$ for the momentum fraction, polarized moment, and trasversity moment, which include a derivative. We will refer to this method as the *two-state fit method*.

In this work, we consider agreement among the above three methods yielding the same value for $\mathcal{M}$ as our criterion that excited states are sufficiently damped out.

If one has ground state dominance, the nucleon matrix elements of the scalar, axial, and tensor local operators at zero momentum transfer and Euclidean time are related to the ratio as follows:

$$\begin{aligned} \Pi_S(\Gamma^4) &= \frac{g_S}{2} \\ \Pi_A^j(\Gamma_k) &= -i\delta_{jk}\frac{g_A}{2} \\ \Pi_T^{ij}(\Gamma_k) &= \epsilon_{ijk}\frac{g_T}{2}. \end{aligned} \tag{30}$$

The corresponding expressions for the vector, axial, and tensor one-derivative operators are

$$\begin{aligned} \Pi_V^{44}(\Gamma^4) &= -\frac{3m_N}{4}\langle x\rangle_{u\pm d} \\ \Pi_V^{kk}(\Gamma^4) &= \frac{m_N}{4}\langle x\rangle_{u\pm d} \\ \Pi_A^{j4}(\Gamma_k) &= -\frac{i}{2}\delta_{jk}m_N\langle x\rangle_{\Delta u\pm\Delta d} \\ \Pi_T^{\mu\nu\rho}(\Gamma_k) &= i\epsilon_{\mu\nu\rho k}\frac{m_N}{8}(2\delta_{4\rho} - \delta_{4\mu} - \delta_{4\nu})\langle x\rangle_{\delta u\pm\delta d}. \end{aligned} \tag{31}$$

Note that after symmetrization and subtraction of the trace as indicated in Eq. (5), only one of the two expressions for $\langle x\rangle_{u\pm d}$ is independent.

For the case of the pion, we only present $\langle x\rangle^{\pi^\pm}_{u-d}$. We consider the largest sink-source separation possible on each lattice, namely, $t_s - t_0 = T/2$. This is possible for the pion since its two point function has constant signal to noise ratio independently of $t_s - t_0$. Therefore, we extract the pion momentum fraction using the plateau method at this single value of the sink-source separation,

$$R^{\pi}(t_s, t_{\mathrm{ins}}) \xrightarrow[\Delta(t_s - t_{\mathrm{ins}})\gg 1]{\Delta(t_{\mathrm{ins}} - t_0)\gg 1} \Pi^{\pi}, \tag{32}$$

where we use Δ to generically denote the energy gap between the energy of the first excited state and the ground state of the hadron of interest in its rest frame. Given ground state dominance, the pion momentum fraction is at zero momentum transfer and Eucledian time obtained from the ratio via

$$\Pi^{\pi} = \frac{m_\pi}{2}\langle x\rangle^{\pi^\pm}_{u-d}. \tag{33}$$

IV. SIMULATION DETAILS

We use the (maximally) twisted mass fermion (TMF) formulation of lattice QCD [41], which is particularly suited for hadron structure calculations since it provides automatic $\mathcal{O}(a)$ improvement requiring no operator modification [42–45]. Twisted mass ensembles with two degenerate flavors of light sea quarks ($N_f = 2$) as well as ensembles including the strange and charm sea quarks ($N_f = 2 + 1 + 1$) are produced by the European Twisted Mass Collaboration (ETMC) and technical details on the simulations can be found in Refs. [46–48] and [49], respectively. This work focuses on the analysis of gauge configurations produced using two degenerate flavors of twisted mass light sea quarks ($N_f = 2$) including a clover term. For the gauge action, we use the Iwasaki action. The parameters of the four ensembles considered in this work are given in Table I. More details on the choice of action and the simulations are given in Refs. [21,50,51].

For the nucleon structure observables, we analyze the ensemble with $a\mu = 0.0009$. We will refer to this ensemble as the physical ensemble and speak in what follows of the *physical point*. For the case of the pion momentum fraction, we use all four ensembles of the TMF with a clover term.

Although the observables of interest in this work are dimensionless and do not depend on the lattice spacing, it is useful to study their dependence on the pion mass, which is a dimensionful quantity. In Ref. [21], the lattice spacing for the new $N_f = 2$ ensembles with the clover term was determined using gluonic quantities as well as the pion and kaon decay constants. Another determination of the lattice spacing mentioned in Ref. [21] is via the nucleon mass.

TABLE I. Input parameters of our new lattice ensembles used in this work. For each ensemble, we give the lattice size, the bare quark mass ($a\mu$), and the corresponding pion mass (m_π). These ensembles use the TMF at one value of β with a clover term with $c_{\mathrm{SW}} = 1.57551$. The lattice spacing given in the table is determined using the nucleon mass as explained in the text.

$\beta = 2.1$, $a = 0.093(1)$ fm, $r_0/a = 5.32(5)$			
$24^3 \times 48$, $L = 2.23$ fm	$a\mu$	0.006	0.003
	m_π (GeV)	0.338(9)	0.244(8)
$32^3 \times 64$, $L = 2.97$ fm	$a\mu$	0.006	
	m_π (GeV)	0.335(9)	
$48^3 \times 96$, $L = 4.46$ fm	$a\mu$	0.0009	
	m_π (GeV)	0.1312(13)	

The physical value of the nucleon mass was used as an input for the determination of the lattice spacings in our previous analysis of the $N_f = 2$ [22,52] and $N_f = 2 + 1 + 1$ [53] twisted mass ensembles. Each set of $N_f = 2 + 1 + 1$ and $N_f = 2$ ensembles involved three values of the lattice spacing. Since those simulations involved larger than physical light quark masses, a chiral extrapolation was needed. We used the lowest-order heavy baryon chiral perturbation theory expression, given by [54]

$$am_N = am_N^0 - 4(c_1/a)(am_\pi)^2 - \frac{3g_A^2}{16\pi(af_\pi)^2}(am_\pi)^3, \tag{34}$$

which is well established within baryon chiral perturbation theory. m_N^0 is the value of the nucleon mass in the chiral limit, and $-4c_1$ gives the σ-term written in units of the lattice spacing. The fit was constrained to reproduce the physical nucleon mass, by fixing the value of c_1. Including an a^2-term in Eq. (34) had a negligible effect on the fit showing that indeed cutoff effects are small [53] for lattice spacings smaller than 0.1 fm. This justified the utilization of continuum chiral perturbation theory to determine the three lattice spacings for each $N_f = 2$ or $N_f = 2 + 1 + 1$ by simultaneously fitting each set of 17 $N_f = 2 + 1 + 1$ or 11 $N_f = 2$ ensembles. The values of the nucleon mass used are taken from Ref. [53] for the $N_f = 2 + 1 + 1$ ensembles and from Ref. [22] for the $N_f = 2$ ensembles. These values of the lattice spacings are used to obtain the pion mass for these ensembles.

For the physical ensemble using the values

$$am_\pi = 0.06196(9) \qquad am_N = 0.440(4), \tag{35}$$

and assuming that we are exactly at the physical point, we find $a = 0.0925(8)$ fm where the average nucleon mass $m_N = 0.939$ GeV is used as an input. With this lattice spacing, we find $m_\pi = 0.1323(12)$ MeV, where the largest part of the error comes from the error on the lattice spacing. This is about 5% less than the average physical pion mass. Using the values of Eq. (35), we find for the ratio $m_N/m_{\pi^\pm} = 7.10(6)$ compared to the physical value of $0.939/0.138 = 6.8$, which again differs by less than 5% from the physical value. In order to check what the effect of a possible small mismatch in the pion mass would be on the lattice spacing, we use the fit extracted from the $N_f = 2+1+1$ ensembles to interpolate to the physical value of pion mass. This is done by making a combined fit of the 17 $N_f = 2+1+1$ ensembles with their three lattice spacings and the lattice spacing for the physical ensemble as well as m_N^0 as fit parameters. The fit yields $\chi^2/\text{d.o.f} = 1.6$ for $\text{d.o.f} = 12$, which is a reasonable value. We find a value of $a = 0.093(1)$ fm for the physical ensemble, consistent with the determination using Eq. (35), while the lattice spacings for the $N_f = 2+1+1$ remain unchanged compared to the values obtained when the physical ensemble was not included. Using $a = 0.093(1)$, we find $m_{\pi^\pm} = 0.1312(13)$ GeV, which is consistent with the value extracted from Eq. (35). Excluding from the fit pion masses larger than 300 MeV yields consistent results for the lattice spacings of the $N_f = 2+1+1$ ensembles, while it does not change the value of the lattice spacing at the physical point. We note that if we fit using the $N_f = 2$ ensembles [22,52] instead of the $N_f = 2+1+1$ ensembles, the value of $a = 0.093(1)$ fm is unchanged. This indicates that the mild interpolation is very robust. In Fig. 2, we show the ratio of the nucleon to pion mass $m_N/m_{\pi^\pm}$, which is a dimensionless observable determined purely from lattice quantities. We note that the values of the lattice spacings affect only the determination of the pion mass plotted as the x axis. The curve shown in Fig. 2 is the fit to the ratio performed on the 17 $N_f = 2+1+1$ ensembles alone. The resulting chiral fit using $m_\pi < 500$ MeV yields $\chi^2/\text{d.o.f} = 1.4$ and describes very well the data. In the figure, we also include the values for the ratio for the $N_f = 2$ ensembles, which also fall on the same curve. This can be taken as an indication that indeed strange and charm sea quark effects are small for the nucleon sector. The consistency of our new result is demonstrated in Fig. 2 by the fact that the ratio $m_N/m_{\pi^\pm}$ for our physical ensemble falls on the curve determined from fitting the $N_f = 2+1+1$ alone. Figure 2 provides a nice demonstration of the negligible effect of lattice artifacts on the $m_N/m_{\pi^\pm}$ ratio.

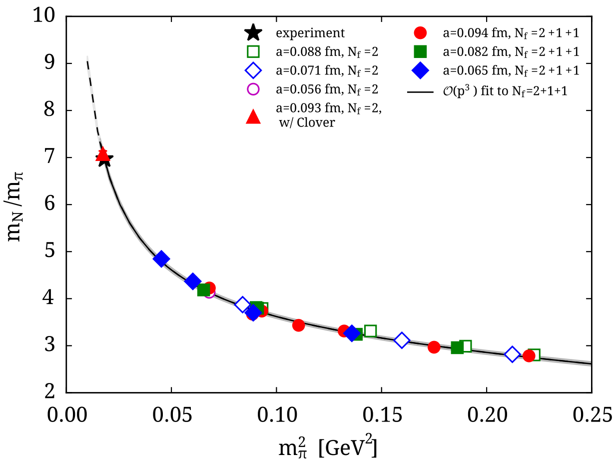

FIG. 2 (color online). The ratio of the nucleon mass to the pion mass as a function of the pion mass squared. For determining the pion mass squared, the scale is set using the nucleon mass at the physical point as described in the text. The fit only used the $N_f = 2+1+1$ ensembles without a clover term (filled circles, diamonds, and squares). The plot also shows the $N_f = 2$ TMF results (open circles, diamonds, and squares) and the $N_f = 2$ ensemble with a clover term at the physical point (filled triangle). For the latter action ($N_f = 2$ with a clover term), we restrict our analysis of nucleon observables to the ensemble simulated at a physical value of the pion mass only.

We note that the value of the lattice spacing determined from the nucleon mass analysis is fully consistent with the one determined from gluonic quantities such as the one related to the static quark-antiquark potential, r_0, and the ones related to the action density renormalized through the gradient flow. It is, however, larger by about 1% as compared to that extracted using f_π [21]. This was also observed in our analysis of $N_f = 2$ and $N_f = 2+1+1$ TMF ensembles [55]. In Table II, we collect the lattice spacings for all the TMF ensembles determined using the nucleon mass and Eq. (34). We take as a systematic error due to the chiral extrapolation the shift in the mean value when discarding ensembles with pion mass greater than 300 MeV. For completeness, we also give the values of r_0 determined from the nucleon mass in the same way as the lattice spacings, although they are not needed in this work. In what follows we use, for the physical ensemble, the

TABLE II. The lattice spacing and value of the scale parameter, r_0 [56], for the $N_f = 2$ and $N_f = 2+1+1$ TMF ensembles as well as for the new $N_f = 2$ TMF ensembles with the clover term, determined using the nucleon mass as explained in the text. The first error is statistical. The second error is the difference in the value when discarding ensembles with pion mass larger than 300 MeV.

$N_f = 2$			
β	3.9	4.05	4.2
a (fm)	0.088(2)(2)	0.071(2)(1)	0.056(2)(1)
r_0 (fm)	0.458(10)(1)	0.467(12)(7)	0.465(13)(7)
$N_f = 2+1+1$			
β	1.90	1.95	2.1
a (fm)	0.094(1)(2)	0.082(1)(2)	0.065(1)(1)
r_0 (fm)	0.501(7)(9)	0.492(6)(3)	0.499(6)(5)
$N_f = 2$ with $c_{\text{SW}} = 1.57551$			
β	2.1		
a (fm)	0.093(1)(0)		
r_0 (fm)	0.493(5)(0)		

value $a = 0.093(1)$. The lattice spacings given in Table II are used to convert the pion mass to physical units. No other physical quantity presented in this work is affected by the value of the lattice spacings.

V. RESULTS

For the nucleon observables, we analyze 96 gauge field configurations with 16 randomly chosen positions for each configuration yielding a total of 1536 measurements. For the nucleon observables, we use three sink-source separations for both the plateau and the summation methods, namely, $t_s/a = 10$, 12, and 14, corresponding to approximately 0.9 fm, 1.1 fm, and 1.3 fm. For all separations, we have 1536 measurements, by computing the required two- and three-point correlation functions. The first results on these quantities were presented in Refs. [57,58]. For the pion, we use the largest possible time separation, namely, $T/2$.

A. Renormalization

We determine the renormalization functions for the lattice matrix elements nonperturbatively, in the RI′-MOM scheme employing a momentum source [59]. For the computation of the renormalization functions of the $N_f = 2+1+1$ ensembles, we employed $N_f = 4$ simulations for at least three different values of the pion mass taking the chiral limit. A similar analysis was performed for the $N_f = 2$ TMF ensembles as well as for our new $N_f = 2$ TMF ensembles that include the clover term using the ensembles with $a\mu = 0.006$, 0.003, and 0.0009, the latter being at the physical pion point. In Refs. [60,61], we carried out a perturbative subtraction of $\mathcal{O}(a^2)$ terms that subtracts the leading cutoff effects yielding only a very weak dependence of the renormalization factors on $(ap)^2$ for which the $(ap)^2 \to 0$ limit can be reliably taken. In this work, we reduce even further the $\mathcal{O}(a^2)$ contributions by subtracting lattice artifacts computed perturbatively to one loop and to all orders in the lattice spacing, $\mathcal{O}(g^2 a^\infty)$, so that we eliminate a large part of the cutoff effects. In Fig. 3, we show the results on the axial and tensor renormalization functions after subtraction. As can be seen, lattice artifacts are practically removed allowing a robust extrapolation to $(ap)^2 = 0$. Due to the good quality of the plateaus after the subtraction of the $\mathcal{O}(g^2 a^\infty)$, any choice for the fit within the nonperturbative region $(ap)^2 \in (2-7)$ yields consistent results. Details on this computation can be found in Ref. [62].

Our previous chiral extrapolations have shown that for all renormalization functions except Z_P, the pion mass dependence is very weak. For the physical ensemble, we compute Z_P for three pion masses corresponding to $a\mu = 0.006$, 0.003, and 0.0009 and performed the pole subtraction. Our value is given in Table III [62]. The scheme and scale-dependent renormalization functions are converted in the $\overline{\text{MS}}$ scheme at a scale of 2 GeV, using the intermediate renormalization group invariant scheme.

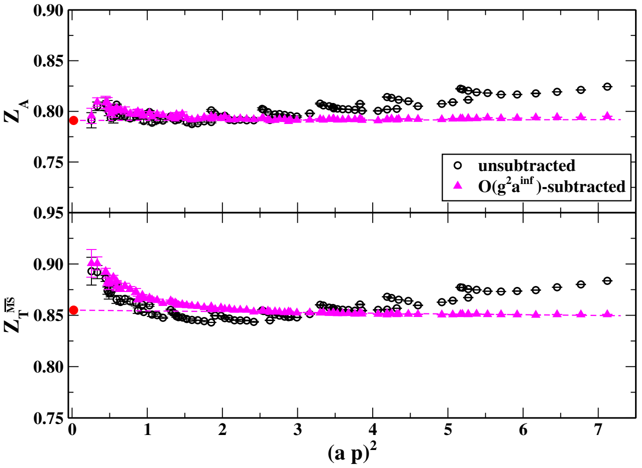

FIG. 3 (color online). Results for the axial (upper) and tensor (lower) renormalization functions versus the momentum square in lattice units. The open (black) circles are the unsubtracted results, while the filled triangles (magenta) show the data after $\mathcal{O}(g^2 a^\infty)$-terms are subtracted. The filled (red) circle at $(ap)^2 = 0$ is the value extracted by fitting to the plateau region [2-7] the subtracted data.

We collect the values of all relevant renormalization functions in Table III, converting the scale-dependent renormalization function in the $\overline{\text{MS}}$ scheme at a scale $\mu = 2$ GeV, which is applicable to all except Z_A. The systematic error is computed by varying the interval for the continuum extrapolation $(ap)^2 \to 0$. The values of Z_P for the $N_f = 2+1+1$ ensembles are taken from Refs. [55,63] where the pole subtraction was performed, while for the new ensembles with the clover term, we use the result of this paper. The values given in Table III are used to renormalize the lattice matrix elements studied in this work. More details are reported in Ref. [62]. For the $N_f = 2$ TMF ensembles without the clover term, we do not calculate the scalar charge and transversity, and therefore the renormalization functions are not given.

The renormalization functions are given for the twisted basis. Going from the twisted to the physical basis affects only the renormalization function for the scalar charge, which, in the twisted basis, is renormalized with Z_P. Furthermore, since disconnected contributions are neglected, the isovector and isoscalar are renormalized using the same renormalization functions. All our results on the scalar and tensor charges and on the moments of PDFs are given in the $\overline{\text{MS}}$ scheme at an energy scale of 2 GeV.

B. Nucleon scalar, axial, and tensor charges

In what follows, we will use the same format to present our results for a given observable in four plots unless otherwise mentioned. Our presentation is illustrated in Fig. 4. In the two upper panels, we present the ratio of Eq. (19), as a function of

TABLE III. Renormalization functions for the ensembles used in this work. They are given in the twisted basis. They are the same in the physical basis except for Z_P, which renormalizes the scalar operator in the physical basis. The renormalization functions for the local axial-vector, scalar, and tensor operators are given in columns 2, 3, and 4, respectively. The three last columns give the renormalization functions for the derivative vector, axial vector, and tensoroperators. The first error is statistical, and the second error is systematic.

β	Z_A	$Z_P^{\overline{\mathrm{MS}}}$	$Z_T^{\overline{\mathrm{MS}}}$	$Z_{DV}^{\overline{\mathrm{MS}}}$	$Z_{DA}^{\overline{\mathrm{MS}}}$	$Z_{DT}^{\overline{\mathrm{MS}}}$
			$N_f = 2$			
3.90	0.769(2)(1)		0.758(2)(4)	1.028(2)(6)	1.102(5)(7)	
4.05	0.787(1)(1)		0.796(1)(3)	1.080(2)(11)	1.161(4)(13)	
4.20	0.791(1)(1)		0.814(1)(3)	1.087(3)(12)	1.164(3)(6)	
			$N_f = 4$			
1.90	0.7474(6)(4)	0.529(7)(45)	0.7154(6)(6)	1.0268(26)(103)	1.1170(54)(223)	1.0965(90)(278)
1.95	0.7556(5)(85)	0.509(4)(37)	0.7483(6)(94)	1.0624(108)(33)	1.1555(36)(289)	1.1727(121)(73)
2.10	0.7744(7)(31)	0.516(2)(29)	0.7875(9)(15)	1.0991(29)(55)	1.1819(47)(147)	1.1822(59)(118)
			$N_f = 2 + c_{\mathrm{SW}}$			
2.10	0.7910(4)(5)	0.5012(75)(258)	0.8551(2)(15)	1.1251(27)(17)	1.1357(20)(205)	1.1472(121)(48)

the insertion time (t_{ins}), shifted by half the sink-source separation, i.e., $t_{\mathrm{ins}} - t_s/2$. This way, the midpoint time of the ratio coincides for all sink-source separations at $t_{\mathrm{ins}} - t_s/2 = 0$. In what follows, all times are measured relative to t_0, and thus we drop the reference to t_0. In the third panel, we show the summed ratio as a function of the sink time, as obtained by Eq. (28), and in the bottom panel, we compare results from the summation method and from the two-state fit method with those obtained by the plateau method.

Let us first discuss the results for the scalar charge shown in Fig. 4. In the two upper panels, we show the ratio for the isoscalar and isovector scalar charges, for the three sink-source separations considered. As explained in the previous section, when the time separations $\Delta t_{\mathrm{ins}} \gg 1$ and $\Delta(t_s - t_{\mathrm{ins}}) \gg 1$, the ratio becomes time independent. Fitting in the plateau region to a constant value, which we refer to as the plateau value, we obtain g_S, as in Eq. (27). This is shown by the blue band in Fig. 4 for $t_s = 14a$. One observes an increasing trend for the plateau value and a clear curvature, especially for the isoscalar, indicating dependence on excited states. Carrying out a two-state fit yields the dashed lines. As in the case of the summation method, the contact points $t_{\mathrm{ins}} = t_0$ and $t_{\mathrm{ins}} = t_s$ are omitted. The value for g_S obtained by the two-state fit is given by the dashed line that spans the entire x range of the figure, with the red band indicating the statistical error, while the result of the summation method is shown with the solid line and gray band indicating the error. As can be seen, within errors, the two-state fit is consistent with the plateau fit but not with the value from the summation method, which, however, carries a very large error indicating the need to increase statistics in order to have a better assessment of the result of this method. In the third panel of Fig. 4, we show the summed ratio for the scalar charge as a function of the sink time, as obtained by Eq. (28), for the isovector and the isoscalar cases. Fitting to a linear dependence with respect to t_s, one extracts the desired matrix element from the slope [Eq. (29)], which is the result shown by the gray band in the two upper graphs of Fig. 4. The width of the bands is obtained by a jackknife resampling of the summed ratio to obtain jackknife errors for the slope, $\mathcal{M}$, and intersection $\mathcal{C}'$ of Eq. (29). The values for g_S from the summation method and those obtained by the plateau method and the two-state fit method are shown in the bottom panel of the figure. One clearly observes the increasing trend of the plateau values with increasing t_s/a as well as the larger values of the summation method shown by the asterisks. This study shows that both larger sink-source time separations as well as larger statistics are needed in order to obtain a meaningful convergence of all methods. This corroborates our findings of our high-statistics analysis of the $N_f = 2+1+1$ TMF ensemble with pion mass 373 MeV, referred to as the B55.32 ensemble, where we showed that $t_s \sim 1.5$ fm is needed [57]. Our current statistics do not allow us to use such a large sink-source separation for the physical ensemble. We note that as a check of the robustness of the two-state fit, we omit more points besides the time slice of the source and the sink. In the case of the scalar charge, taking the fit range $t_{\mathrm{ins}} \in [t_0+2, t_s-2]$ and $t_{\mathrm{ins}} \in [t_0+3, t_s-3]$, we obtain 2.18(34) and 2.22(33), respectively, for the isovector case and 9.68(26) and 9.75(24) for the isoscalar case, which are consistent with 2.16(34) and 9.62(27) extracted when just omitting the source and the sink. Thus, for the scalar charge, the fluctuation of the central value when changing the fit range is within the statistical error and of the order of 2%.

In Fig. 5, we show results for the axial charge following the same notation as that in Fig. 4. For the axial charge, one observes a milder dependence on t_s showing that excited states contributions are suppressed for this observable. Because of this weaker dependence, a two-state fit does not yield a meaningful result for these values of t_s/a, at least within the statistical accuracy of 1536 measurements. We therefore only show results for the plateau and

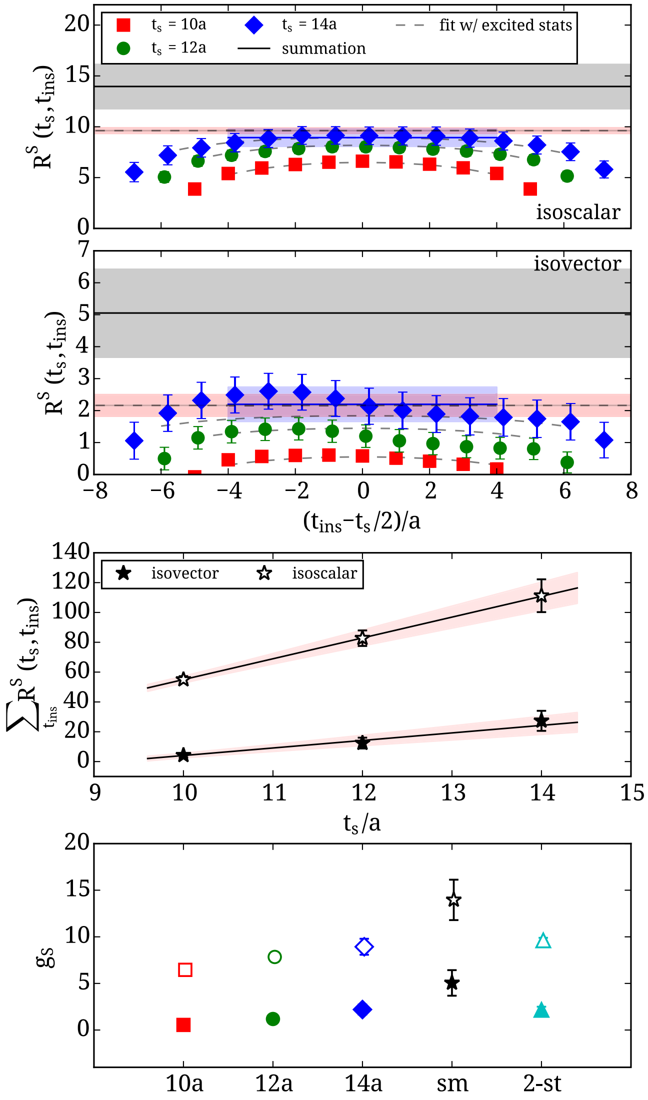

FIG. 4 (color online). Results for the isovector and isoscalar nucleon scalar charge: In the upper two panels is the ratio from which g_S is extracted as a function of $t_{ins} - t_s/2$ for the isoscalar (upper) and the isovector (lower). The blue bands spanning from $(t_{ins} - t_s/2)/a = -4$ to 4 are fits to the ratio for $t_s/a = 14$. The dashed lines show the result of the two-state fit method. The dashed (solid) line spanning the entire x range shows the value obtained via the two-state (summation) method, with the band indicating the corresponding statistical error. In the third panel, the summed ratio is shown for the isovector (filled symbols) and isoscalar (open symbols) cases. The line shows the result of a linear fit, while the bands show the statistical error based on the jackknife error of the fitted parameters. In the bottom panel, we show the result for g_S when using the plateau method with $t_s/a = 10$, 12, and 14 (squares, circles, and rhombuses, respectively), as well as when using the summation method denoted by "sm" (asterisks) and the two-state fit "2-st." (triangles).

summation methods. The values from the plateau method do not vary as a function of t_s and are in agreement with the value extracted from the summation method, within the large statistical uncertainties of the latter.

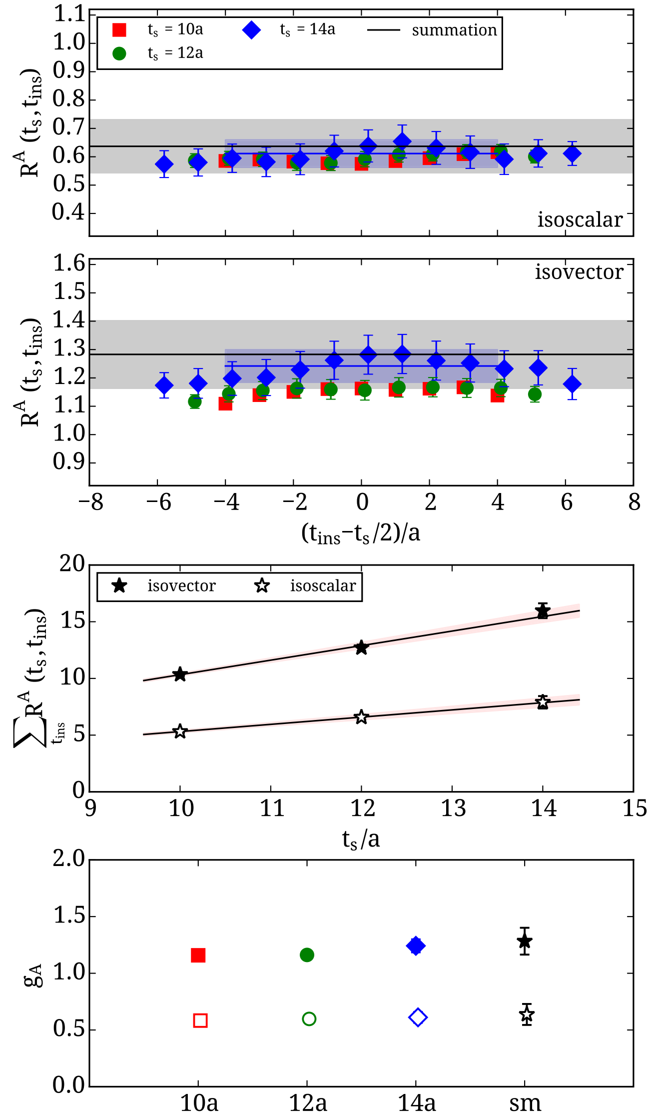

FIG. 5 (color online). Results for the axial charge. The notation is the same as that in Fig. 4.

Our results for the tensor charge (g_T) are shown in Fig. 6. The dependence of g_T on t_s is similar to that observed in the case of g_A, and thus a two-state fit fails to accurately resolve the excited states. Thus, we only compare the results extracted using the summation and plateau methods in the bottom panel. As can be seen, g_T exhibits no dependence on the sink-source separation within the current statistical uncertainties, evident by the same values extracted by fitting to the plateau for the three different sink-source separations. The value extracted from the summation method is in agreement but carries a much larger error and thus does not provide a stringent check.

C. Nucleon momentum fraction, helicity, and transversity moments

The momentum fraction is shown in Fig. 7 for the connected isoscalar $\langle x\rangle_{u+d}$ and isovector $\langle x\rangle_{u-d}$

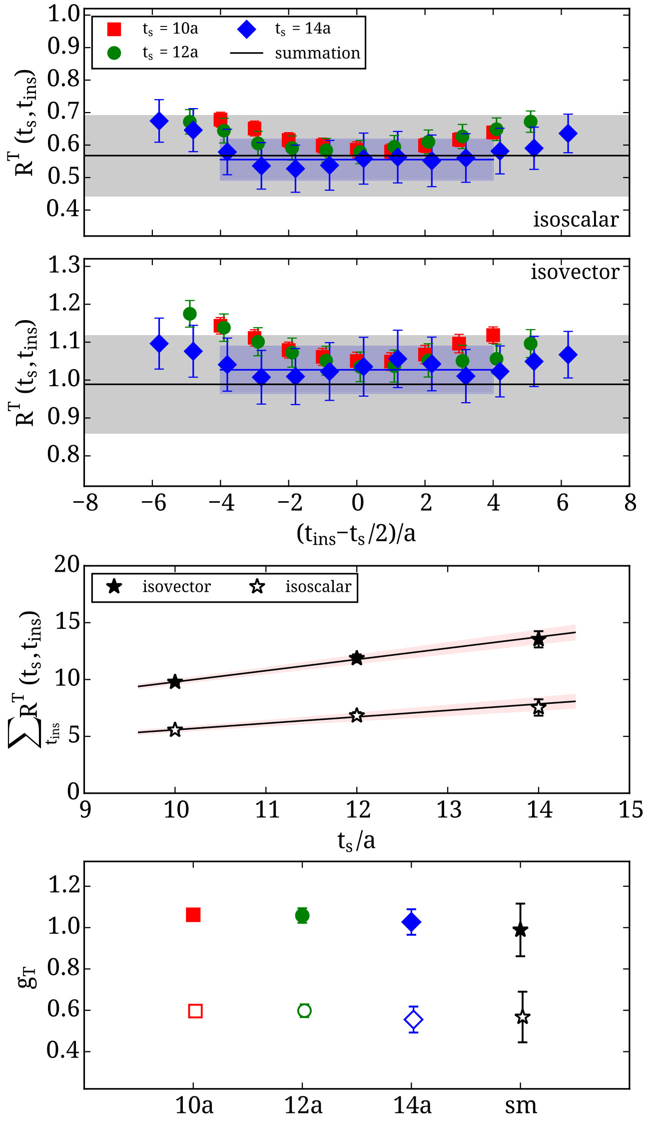

FIG. 6 (color online). Results for the tensor charge. The notation is the same as that in Fig. 4.

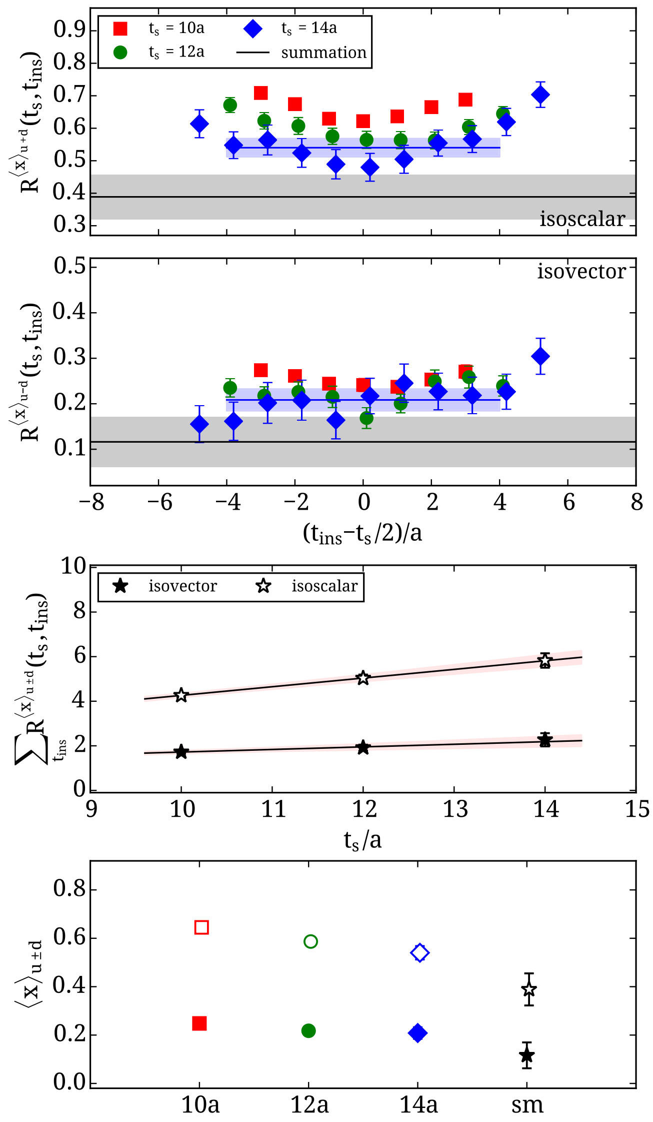

FIG. 7 (color online). Results for the momentum fraction. The notation is the same as that in Fig. 4.

combinations. Both isoscalar and isovector channels exhibit excited-state contributions, especially for the isoscalar channel. A two-state fit is performed using $t_{ins} \in [t_0+2, t_s-2]$, which, however, yields too large errors to include in the plots (see Table IV). Using $t_{ins} \in [t_0+3, t_s-3]$, we find a value of 0.48(19) for the isoscalar, which is consistent with the value given in Table IV. For the isovector, both fit ranges yield consistent results albeit with a large error that does not allow us to access the sensitivity on the fit range. Furthermore, as can be seen in the lowest panel of Fig. 7, a decreasing trend is observed as the sink-source separation is increased from $10a$ to $14a$, showing that elimination of excited-state effects is responsible for reducing the value of this matrix element. The summation method yields a value that is even lower but with a large statistical uncertainty. Like for the case of the scalar charge, a larger value of t_s/a and increased statistics will be needed to reach consistency among the various methods with meaningful errors.

The helicity moment $\langle x\rangle_{\Delta u\pm\Delta d}$ and transversity moment $\langle x\rangle_{\delta u\pm\delta d}$ are shown in Figs. 8 and 9. For both isoscalar observables, a milder dependence on the sink-source separation is observed. This is also true for the isovector transversity moment. On the other hand, the isovector helicity moment shows a decreasing trend similar to that observed in the case of the isovector momentum fraction. The value obtained using the summation method is consistent in all cases with the plateau value when $t_s/a = 14$, albeit with a large statistical uncertainty.

The nucleon results presented in Figs. 4–6 and Figs. 7–9 are summarized in Table V, where we give the values obtained when using the plateau method and the summation method. Our results with sink-source time separation $12a$, $14a$, and the summation method agree within one to

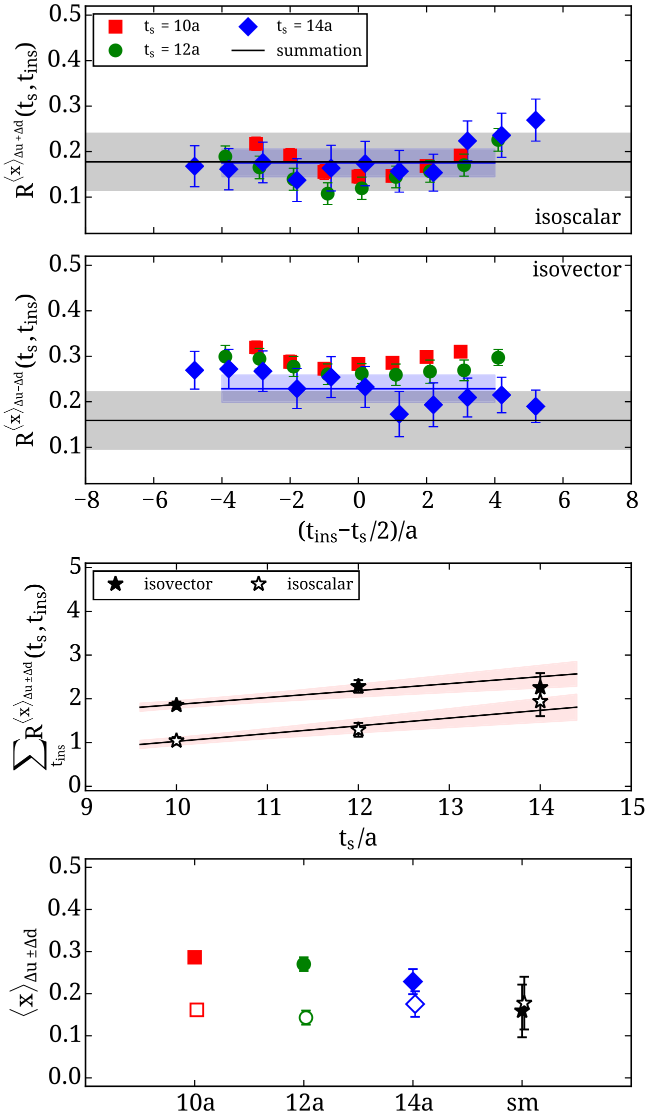

FIG. 8 (color online). Results for the nucleon helicity moment. The notation is the same as that in Fig. 4.

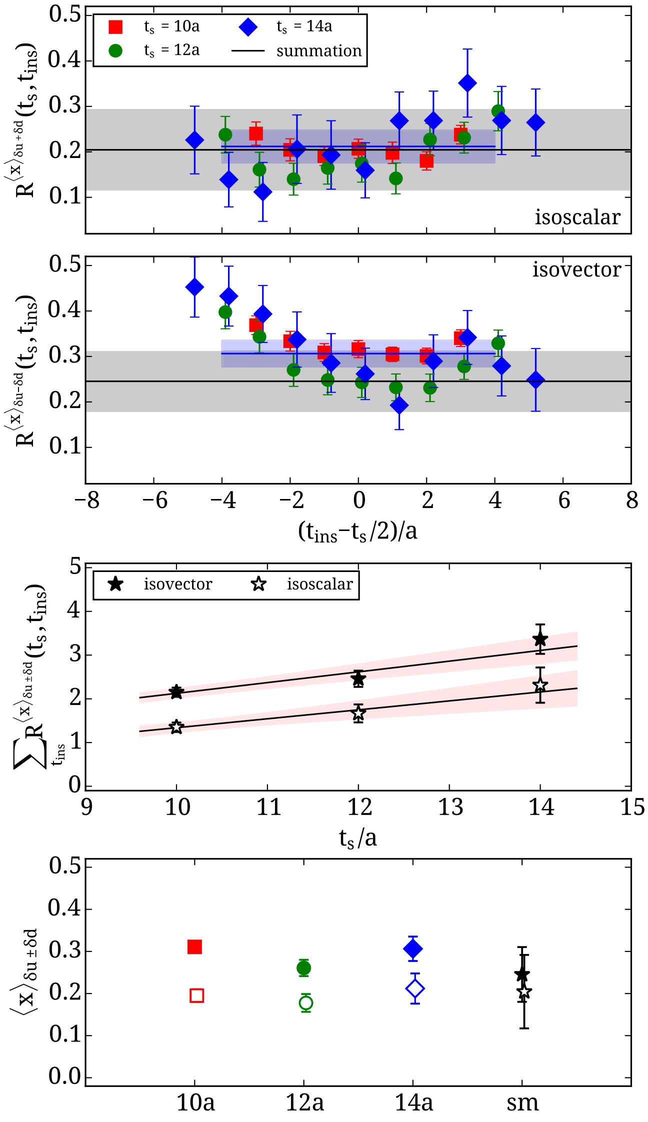

FIG. 9 (color online). Results for the transversity moment. The notation is the same as that in Fig. 4.

two standard deviations. The errors exhibited by the summation method, however, are still large, which is explained by the fact that this method relies on a two parameter fit, contrary to the plateau method which is a fit to a constant. Nevertheless, within our current statistics, the summation method can provide an additional check of excited-state effects.

We observe that the scalar charge g_S and momentum fraction $\langle x\rangle_{u\pm d}$ exhibit non-negligible excited state effects when increasing the sink-source separation. For these cases, we show in Table IV the results when employing the two-state fit method. For both observables, the two-state fit result agrees with the plateau method for $t_s/a = 14$.

In Table VI, we give our results for the isovector quantities as determined from the plateau method using $t_s \sim 1.3$ fm, as well as for the up- and down-quark contributions neglecting disconnected diagrams. We note that for the up- and down-quark contributions of these quantities, we carry out the complete analysis with jackknife resampling starting from three-point correlation functions with only an up- or down-quark insertion. Alternatively, one can form linear combinations of the final isovector and isoscalar results of Table V, which will give consistent up- and down-quark contributions within statistical errors. Except for the scalar and the momentum fraction, the results of Table VI are in agreement with the value obtained using the summation method. For the scalar and the momentum fraction, they are consistent with the result extracted using the two-state fit albeit with large statistical error especially for the momentum fraction. Since for the scalar there are large differences still between the results at different values of t_s as well as from the value extracted using the summation method, we do not include a single value in the table.

TABLE IV. Results for the nucleon scalar charge and momentum fraction when employing the two-state fit.

Moment	Isovector	Isoscalar
g_S	2.16(34)	9.62(27)
$\langle x\rangle_q$	0.19(24)	0.50(20)

Our TMF results for the three isovector charges g_S^{u-d}, g_A^{u-d}, and g_T^{u-d} and moments $\langle x\rangle_{u-d}$, $\langle x\rangle_{\Delta u-\Delta d}$, and $\langle x\rangle_{\delta u-\delta d}$ are collected in Figs. 10 and 11. In the Appendix, we give our updated results for our high-statistics analysis of the B55.32 ensemble for several sink-source separations as well as for one $N_f = 2+1+1$ ensemble at a finer lattice spacing [26]. These results use the new renormalization functions given in Table III. For g_A^{u-d}, $\langle x\rangle_{u-d}$, and $\langle x\rangle_{\Delta u-\Delta d}$, we include results using $N_f = 2$ at three lattice spacings and, for one mass, at two different volumes [22,23]. These are given with the new renormalization functions in the Appendix. These results show that cutoff effects are small for lattice spacings smaller than 0.1 fm. Finite volume effects are not visible within our statistical accuracy when comparing results for two ensembles simulated at a pion mass of about 300 MeV and $Lm_\pi = 3.3$ and $Lm_\pi = 4.6$. For the physical ensemble, we show results for $t_s = 12a \simeq 1.1$ fm and $t_s = 14a \simeq 1.3$ fm and from using the summation method. We expect $\langle x\rangle_{u-d}$ to have moderate excited states contamination as revealed by our high-statistics investigation of $\langle x\rangle_{u-d}$ for the $N_f = 2+1+1$ ensemble with $m_\pi = 373$ MeV that showed that its value decreases

TABLE V. Results for the nucleon charges and first moments computed with the physical ensemble. The first column denotes the observable, with $u-d$ indicating the isovector contribution and $u+d$ the connected isoscalar. Results extracted using the plateau method are given for $t_s/a = 10$, 12 and $t_s/a = 14$ in the second, third, and fourth columns. The value extracted using the summation method is given in the last column. The errors are obtained using jackknife.

	Plateau			Summation
Moment	10*a*	12*a*	14*a*	method
g_S^{u+d}	6.46(27)	7.84(48)	8.93(86)	14.0(2.2)
g_S^{u-d}	0.55(18)	1.18(34)	2.20(54)	5.0(1.4)
g_A^{u+d}	0.583(14)	0.597(23)	0.611(48)	0.637(92)
g_A^{u-d}	1.158(16)	1.162(30)	1.242(57)	1.28(12)
g_T^{u+d}	0.596(21)	0.598(31)	0.555(63)	0.57(12)
g_T^{u-d}	1.062(21)	1.058(35)	1.027(62)	0.99(13)
$\langle x\rangle_{u+d}$	0.645(13)	0.587(18)	0.540(28)	0.389(66)
$\langle x\rangle_{u-d}$	0.248(09)	0.218(15)	0.208(24)	0.116(54)
$\langle x\rangle_{\Delta u+\Delta d}$	0.161(12)	0.143(17)	0.175(30)	0.177(63)
$\langle x\rangle_{\Delta u-\Delta d}$	0.286(11)	0.270(16)	0.229(33)	0.159(62)
$\langle x\rangle_{\delta u+\delta d}$	0.195(15)	0.178(21)	0.212(36)	0.204(87)
$\langle x\rangle_{\delta u-\delta d}$	0.311(13)	0.261(19)	0.306(29)	0.245(65)

TABLE VI. Results for the nucleon axial and tensor charges and first moments of parton distributions. In the first column, we give the observable, in the second the isovector combination, and in the third and fourth the u and d values neglecting disconnected contributions.

	Isovector	Up	Down
g_A	1.242(57)	0.926(47)	−0.315(24)
g_T	1.027(62)	0.791(53)	−0.236(33)
$\langle x\rangle_q$	0.208(24)	0.373(22)	0.166(13)
$\langle x\rangle_{\Delta q}$	0.229(30)	0.202(26)	−0.027(16)
$\langle x\rangle_{\delta q}$	0.306(29)	0.264(25)	−0.045(21)

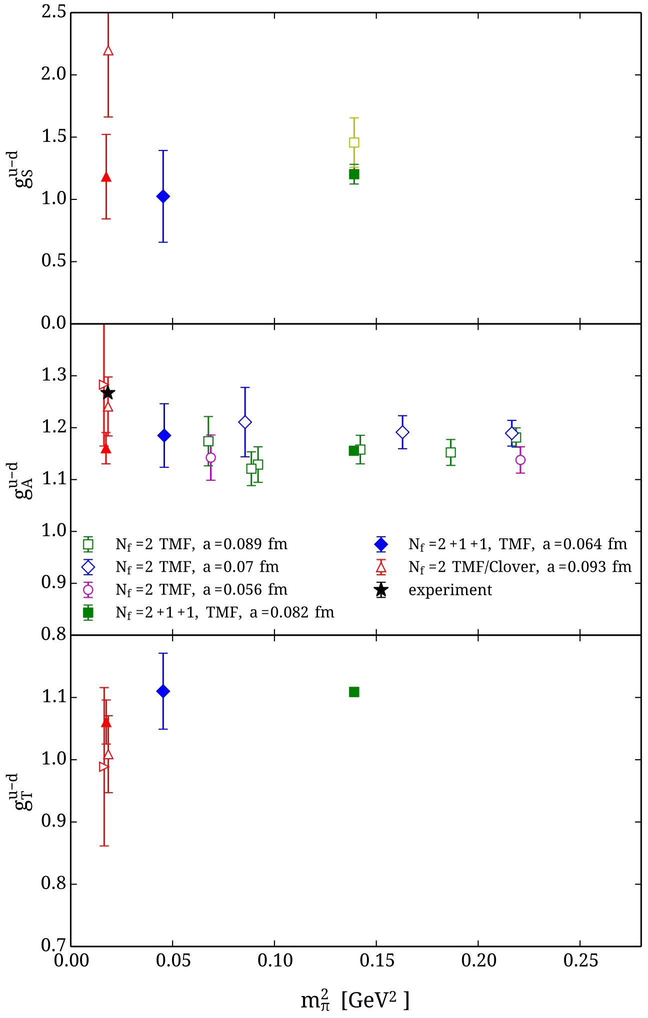

FIG. 10 (color online). Isovector nucleon scalar charge g_S^{u-d} (upper), axial charge g_A^{u-d} (middle), and tensor charge g_T^{u-d} (lower) using the values of Table VI. TMF results are shown for i) $N_f = 2$, $a = 0.089$ fm (open green squares), $a = 0.07$ fm (open blue diamonds), and $a = 0.056$ fm (open magenta circles); ii) $N_f = 2+1+1$, $a = 0.082$ fm (filled green squares), and $a = 0.064$ fm (filled blue diamonds); and iii) $N_f = 2$ TMF clover-improved $a = 0.093$ fm (physical ensemble), $t_s/a = 12$ (filled red triangle), $t_s/a = 14$ (open red triangle), and the summation method (open right triangle). The physical value is shown with the black asterisk. For the scalar charge, we show with the open yellow square the value when $t_s \sim 1.5$ fm.

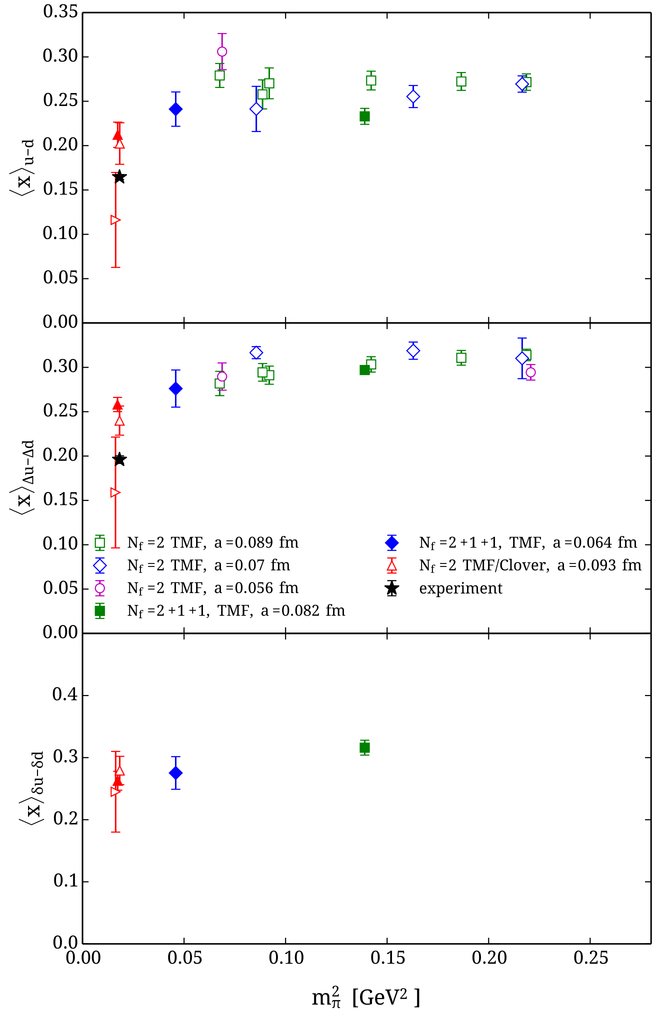

FIG. 11 (color online). Isovector nucleon momentum fraction $\langle x\rangle_q$ (upper), helicity $\langle x\rangle_{\Delta q}$ (middle), and transversity $\langle x\rangle_{\delta q}$ (lower). The notation is the same as that in Fig. 10.

with increasing t_s [25]. Our current results at the physical point with 1536 statistics have much larger errors as compared to what was achieved in Ref. [25], but there is a clear decreasing trend as we increase t_s. For the scalar charge, the excited-state contributions are large, as can be seen both from the results obtained with the $N_f=2+1+1$ ensemble with 373 MeV where a high-statistics analysis is carried out but also for the physical ensemble where no convergence is achieved with the current sink-source separations and statistics. Although for g_A^{u-d}, $\langle x\rangle_{u-d}$, and $\langle x\rangle_{\Delta u-\Delta d}$ our results from the summation method are in agreement with the experimental values, the errors are still too large and must be reduced by a factor of at least 2 to draw a safe conclusion. However, we stress that our value for g_A^{u-d} from the plateau method using $t_s\sim 1.3$ fm agrees with the experimental value. To our knowledge, this is the first computation for which the value of the axial charge is reproduced from the plateau method, without any chiral extrapolation.

D. Pion momentum fraction

In this section, we present results on the isovector pion momentum fraction. Three $N_f=2$ TMF ensembles with the clover term are analyzed with heavier than physical pion masses, two of which have a spatial lattice size of 2.23 fm and one has a spatial lattice size of 2.98 fm. A fourth ensemble that includes the clover term is simulated using the physical value of the pion mass and spatial lattice extent of 4.46 fm. This is the ensemble used for the nucleon observables, and the ensemble details can be found in Table I. The number of measurements, which are well separated in the number of hybrid Monte Carlo trajectories, is given in Table VII.

In Fig. 12, we show the ratio Eq. (22) as a function of $t_{\rm ins}/a$ for the physical ensemble. The black horizontal line represents the value quoted in Table VII. The statistical accuracy of the pion correlation functions allows for a more careful assessment of systematic uncertainties in the plateau fit as compared to the case of the nucleon. Namely, we obtain the plateau value by performing constant fits to the data with all possible fit ranges with degrees of freedom larger than 5. For each of these fits, a weight factor

$$w=\left(\frac{1-2|p-0.5|}{W}\right)^2\left(\frac{1-2|p_{m_\pi}-0.5|}{W_{m_\pi}}\right)^2$$

is computed, where p (p_{m_π}) is the p-value of the fit and W (W_{m_π}) the statistical error of the fit parameter (of m_π) determined using 1500 bootstrap samples. The pion mass itself is also determined for a large number of fit ranges. The final result is determined as the weighted median over all combinations of fit ranges. The 68.54% confidence interval of the weighted distribution is quoted as the systematic uncertainty.

For the twisted mass value $a\mu=0.006$, we have two spatial lattice sizes available, namely, $L/a=24$ and $L/a=32$. Within errors, the result for $\langle x\rangle_{u-d}^{\pi^\pm}$ agrees

TABLE VII. Results for the renormalized $\langle x\rangle_{u-d}^{\pi^\pm}$ in $\overline{\rm MS}$ at 2 GeV for the four TMF clover-improved ensembles considered in this work. In the first column, we give the bare twisted quark mass, and in the second column the spacial extent in lattice units. In the fourth column, we provide the value of $\langle x\rangle_{u-d}^{\pi^\pm}$ of the pion with its statistical and systematic uncertainty computed as explained in the text. The last column gives the number of measurements for each ensemble.

$a\mu$	L/a	$\langle x\rangle_{u-d}^{\pi^\pm}$ in $\overline{\rm MS}$ at 2 GeV	$N_{\rm meas}$
0.006	24	$0.249(7)(^{+3}_{-3})$	210
0.006	32	$0.259(4)(^{+1}_{-1})$	240
0.003	24	$0.219(13)(^{+6}_{-5})$	276
0.0009	48	$0.214(15)(^{+12}_{-9})$	309

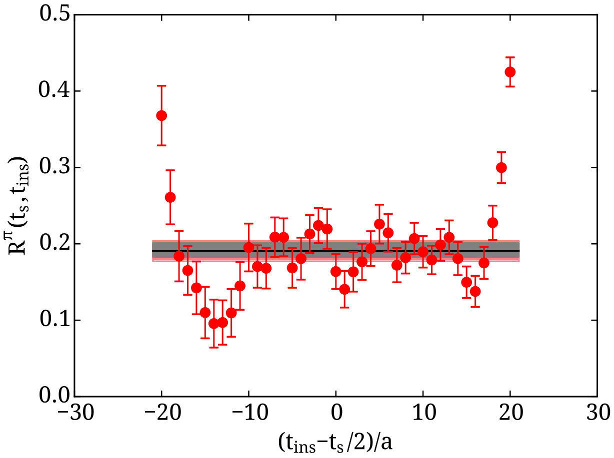

FIG. 12 (color online). The ratio for $\langle x\rangle^{\pi^{\pm}}_{u-d}$ using the $a\mu = 0.0009$ ensemble. We show the weighted median over the different fit ranges as a solid black line, the statistical error as the red band, and the systematic errors as the gray band.

between these two ensembles. We show the $\langle x\rangle^{\pi^{\pm}}_{u-d}$ results for $L/a = 24$ and $L/a = 32$ in Fig. 13 as a function of $t_{\rm ins}/a$.

We compare our $N_f = 2$ clover-improved results with results obtained for $N_f = 2$ twisted mass ensembles without the clover term published in Ref. [36]. These ensembles were simulated using $\beta = 3.90$ with four values of the bare quark mass: $a\mu = 0.004$, 0.0064, 0.0085, and 0.0100. The lattice spacing for these ensembles is 0.089(1) fm, which is similar to the clover-improved ensembles. For $a\mu = 0.004$, we have again two spatial lattice extents $L/a = 24$ and $L/a = 32$ available. As for the clover-improved ensembles, the results for $\langle x\rangle^{\pi^{\pm}}_{u-d}$ agree between the two volumes.

From the comparison of the different available spatial lattice sizes, we conclude that within the current statistical uncertainties we cannot detect significant finite volume effects for $m_\pi L \leq 3.2$ realized for the $\beta = 3.90$, $a\mu = 0.004$, $L/a = 24$ ensemble. The physical ensemble has slightly smaller $m_\pi L = 2.97$, and the clover ensemble with $a\mu = 0.003$ has $m_\pi L = 2.77$. Therefore, we cannot completely exclude finite size effects for these two ensembles. All other ensembles have $m_\pi L > 3.2$. Note that we are currently generating a physical ensemble with $L/a = 64$, which will allow us to check for finite size effects. We expect pion observables to be more sensitive to finite size effects than nucleon observables; having a larger volume will enable us to confirm this expectation.

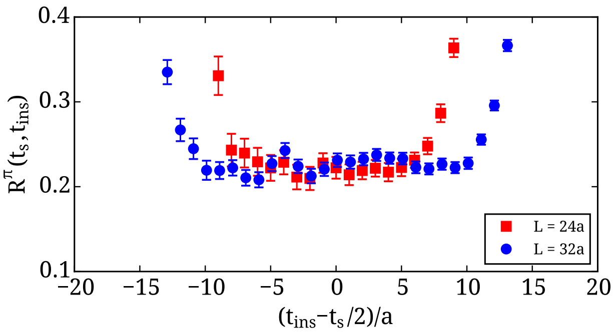

FIG. 13 (color online). The ratio for $\langle x\rangle^{\pi^{\pm}}_{u-d}$ for $a\mu = 0.006$, comparing results obtained for lattices of two sizes: $L = 24a$ (red squares) and $L = 32a$ (blue circles).

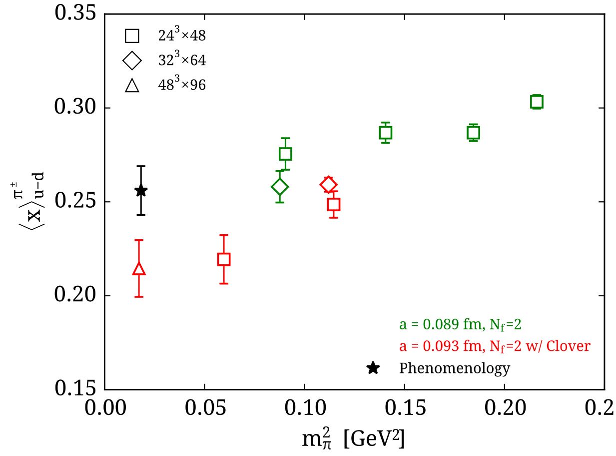

FIG. 14 (color online). The renormalised momentum fraction of the pion $\langle x\rangle^{\pi^{\pm}}_{u-d}$ as a function of the squared pion mass at renormalization scale $\mu = 2$ GeV in the $\overline{\rm MS}$ scheme. The results of this work (red symbols) are shown together with previous results obtained using $N_f = 2$ ensembles (green symbols) [36] compared to the phenomenological value (black star) from Ref. [64]. Results at two values of the pion mass but different lattice volumes are shown by the open squares ($24^3 \times 48$) and diamonds ($32^3 \times 64$).

The results for the renormalized isovector momentum fraction of the pion $\langle x\rangle^{\pi^{\pm}}_{u-d}$ are summarized in Table VII. The renormalization factors used are given in Table III at 2 GeV in the $\overline{\rm MS}$ scheme. The results are also displayed in Fig. 14 as a function of the squared pion mass. In Fig. 14, one observes that there is agreement between the clover-improved and non-clover improved ensembles within errors. Note that systematic uncertainties are not displayed.

In Fig. 14, we compare with the latest phenomenological value for $\langle x\rangle^{\pi^{\pm}}_{u-d}$ which can be found in Ref. [64] and reads

$$\langle x\rangle^{\pi^{\pm}}_{u-d} = 0.256(13).$$

Note that the result given in Ref. [64] is at $\mu = 5.2$ GeV renormalization scale and we have translated it to $\mu = 2$ GeV using three-loop perturbation theory. The phenomenological value is compatible with the value of $0.214(15)(^{+12}_{-9})$ computed for the physical ensemble.

The results presented here can be compared to Ref. [8], where $N_f = 2$ nonperturbatively clover-improved Wilson fermions have been used, including two ensembles with pion mass values around 150 MeV. Two values of the lattice spacing are investigated, $a = 0.06$ and $a = 0.07$ fm, respectivley. In that reference, a bending of the momentum fraction values toward small pion mass values is observed, while the agreement at $m_\pi > 300$ MeV to the results presented here is reasonable.

E. Comparison of nucleon observables with different fermion actions

In this section, we compare our results on nucleon observables with other recent results obtained using simulations with similar parameters.

A number of lattice QCD collaborations are investigating g_A since, as emphasized already, this is considered a benchmark quantity for lattice QCD. In Fig. 15, we show results for $N_f = 2$ [22] and $N_f = 2+1+1$ [26] twisted mass fermions obtained in previous analyses using simulations with pion masses in the range of 450 to 210 MeV for various volumes always satisfying the condition $Lm_\pi > 3$. For $N_f = 2$ ensembles, three values of the lattice spacing were analyzed, namely, $a = 0.089$, 0.07, and 0.056 fm and, at one pion mass of about 300 MeV, for two different volumes. As already pointed out, the consistency among these results indicates small cutoff and finite volume effects. The $N_f = 2$ values are consistent with the values extracted using two $N_f = 2+1+1$ ensembles with lattice spacing $a = 0.082$ fm and $a = 0.064$ fm, showing that there are no visible strange and charm sea quark effects on these quantities at least to the accuracy we now have. This allows a comparison with results using different fermion discretization schemes even before the continuum extrapolation is performed. In Fig. 15, we include results obtained using clover-improved fermions from two collaborations. In Ref. [65], results were obtained using $N_f = 2$ clover fermions with the smallest pion mass of 150 MeV and three lattice spacings $a = 0.08$, 0.07, and 0.06 fm as well as several volumes. These results are in agreement with ours. The LHPC analyzed $N_f = 2+1$ tree-level clover-improved Wilson fermions with 2-HEX stout smeared gauge links provided by the BMW Collaboration using the smallest pion mass of 149 MeV at one lattice spacing $a = 0.116$ fm [66]. These tend in general to have lower values. This is particularly severe close to the physical pion mass. LHPC also computed the axial charge in a mixed action approach that uses DWF on staggered sea quarks by LHPC [67] with $a = 0.124$ fm where high accuracy results were produced for heavier pion masses. These results are in good agreement with ours. We note that both TMF and clover-improved results are extracted using the plateau method with a sink-source time separation of about 1 to 1.2 fm with the exception of our result for the physical ensemble where we used time separations of up to 1.3 fm. In addition, results at two pion masses using a hybrid action with clover valence on $N_f = 2+1+1$ staggered fermions used a two-state fit [68] and are included here for comparison. They tend to be higher than other results, although they are compatible with our $N_f = 2+1+1$ value at a pion mass of about 210 MeV, which albeit carries a large error. The general conclusion is that the lattice results for pion mass higher than about 300 MeV, which are more accurate as compared to those at smaller pion masses, are in agreement. This is an indication that lattice systematics are under control in this pion mass range. Results for pion masses smaller than about 300 MeV, in general, have larger statistical errors, and agreement among them is harder to assess. They clearly indicate the need for more precise values and a reliable assessment of systematic uncertainties. This is particularly relevant for the results close to the physical point where we observe a disagreement between clover results from LHPC at a pion mass of 149 MeV and from Ref. [65] at a similar pion mass. This discrepancy was claimed to be due to excited states, which were shown to be suppressed with improved smearing in Ref. [65]. This needs to be further investigated with a dedicated precision calculation with a complete assessment of systematic uncertainties. Other results using clover-improved fermions not shown here are those by the CLS Collaboration [40], which extracted their values from the summation method. A complete set of the results on g_A can be found in Ref. [4]. The result of this work is shown with the open triangle obtained for $t_s = 1.3$ fm. This value is in agreement with the experimental value with, however, admittedly a rather large error.

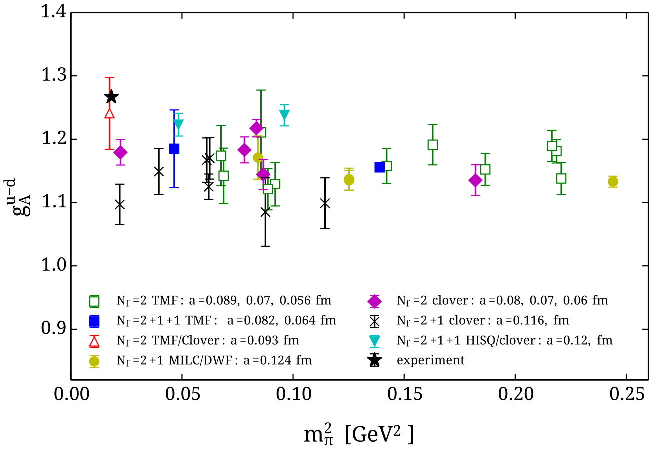

FIG. 15 (color online). Results for the nucleon axial charge for different fermion actions. Twisted mass fermion results are shown with open green squares for $N_f = 2$ ensembles [22], with filled blue squares for $N_f = 2+1+1$ [26], and with the open red triangle for the physical ensemble using the plateau value at $t_s/a = 14$ (see Table VI). Results are also shown using $N_f = 2$ clover fermions (filled purple diamonds) [65]; $N_f = 2+1+1$ staggered sea and clover valence quarks (filled light blue inverted triangles) [68]; $N_f = 2+1$ with domain wall fermions on a staggered sea (filled yellow circles) [67]; and $N_f = 2+1$ clover (black x symbols) [66].

The calculation of the scalar and tensor charges has received more attention recently due to their relevance for searches of new scalar and tensor couplings beyond the familiar weak interactions of the Standard Model in the decay of ultracold neutrons. We compare our TMF results in Fig. 16 with those obtained by three groups of which the results on the nucleon axial charge were also included in Fig. 15. The first set of results is from Ref. [65] using

$N_f = 2$ clover fermions at three lattice spacings. The second set is from the LHPC group which in Ref. [69] used $N_f = 2+1$ clover with 2-HEX stout smeared gauge links at lattice spacings $a = 0.116$ fm and $a = 0.09$ fm, $N_f = 2+1$ DWF with $a = 0.084$ fm, and a hybrid action of DWF on staggered sea with $a = 0.124$ fm. Both these groups used the plateau method and sink-source time separation within 1 to 1.2 fm. The third set of results is from Ref. [68] at one lattice spacing for the scalar and from Ref. [70] at three lattice spacings for the tensor obtained using a hybrid action of DWF on $N_f = 2+1+1$ staggered fermions and employing a two-state fit. For the case of the scalar charge shown in the upper panel of Fig. 16, we observe overall a good agreement among all lattice results obtained with similar sink-source separation. However, our high-statistics analysis using $N_f = 2+1+1$ TMF at pion mass 373 MeV revealed excited states contamination, which only becomes negligible when $t_s \sim 1.5$ fm, increasing the value of g_S. The value extracted when $t_s = 1.48$ fm is shown in Fig. 16 by the open green square. A similar analysis for the physical ensemble also reveals large contributions from excited states for g_S^{u-d}. Comparing results obtained for $t_s \sim 1.1$ and 1.3 fm, we confirm an increasing value as we increase t_s. However, the statistical error is large despite the fact that we have 1536 measurements as compared to 1200 used for the ensemble at $m_\pi = 373$ MeV. This demonstrates that obtaining the same accuracy at the physical point for $t_s \sim 1.5$ fm, which may be needed to suppress excited states, requires more than an order of magnitude increase in statistics.

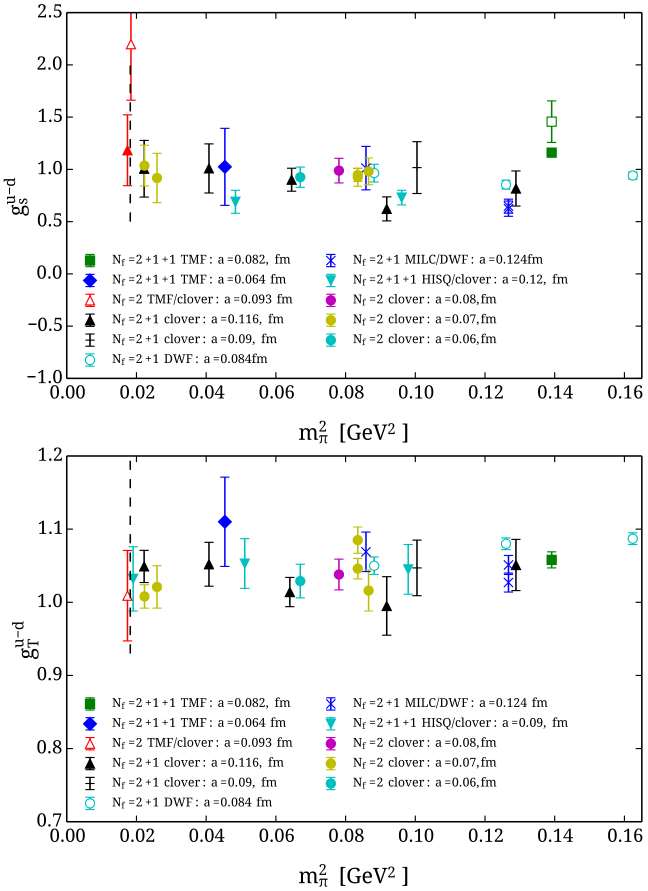

FIG. 16 (color online). Isovector nucleon scalar charge g_S^{u-d} (upper) and tensor charge g_T^{u-d} (lower) vs m_π^2. TMF results are shown for two ensembles of $N_f = 2+1+1$ fermions (filled green square for $t_s \sim 1.15$ fm, open green square for $t_s \sim 1.5$ fm, and filled blue diamond) and for the physical ensemble (filled red triangle for $t_s \sim 1.1$ fm and open red triangle for $t_s \sim 1.3$ fm). Results are also shown using: clover fermions on $N_f = 2+1+1$ staggered sea from Refs. [68,71] for g_S^{u-d} and from Ref. [70] for g_T^{u-d} (filled light blue downward triangles); $N_f = 2+1$ clover (black filled triangles and crosses); $N_f = 2+1$ domain wall fermions (open light blue circles) and hybrid (blue crosses) [69]; $N_f = 2$ clover fermions for three values of the lattice spacing (filled magenta, yellow, and light blue circles crosses) [65]. All results were extracted using the plateau method except those from Refs. [68,70], which used a two-state fit.

Results on the isovector tensor charge are compared in the lower panel of Fig 16. Our TMF results shown in Fig. 10 show that excited-state contributions are less severe for g_T^{u-d} and that the values at $t_s/a = 12$ and $t_s/a = 14$ are consistent. Indeed our value at the physical point obtained using $t_s \sim 1.3$ fm is in very good agreement with other lattice results providing a prediction for this important quantity directly at the physical point.

Recent lattice QCD results have also been obtained for the isovector momentum fraction and helicity. A comparison of our results for $\langle x\rangle_{u-d}$ and $\langle x\rangle_{\Delta u-\Delta d}$ with other collaborations is shown in Fig. 17. We only show results extracted using the plateau method. Most of the analyses employed a sink-source separation of 1 to 1.2 fm including our TMF $N_f = 2$ ensembles. As shown in Ref. [25] where $\langle x\rangle_{u-d}$ was computed using our $N_f = 2+1+1$ ensemble at pion mass of 373 MeV and high statistics, excited states may not be negligible for this observable. Indeed, this is confirmed by our current analysis for the physical ensemble where there is a decreasing trend as t_s increases. Our value at the physical point is in agreement with the other lattice values extracted close to the physical point. These are from Ref. [72], which is an update of Ref. [73] for $m_\pi \sim 160$ MeV and from LHPC at $m_\pi \sim 150$ MeV using $N_f = 2+1$ clover fermions with 2-HEX smeared gauge action [66]. Our value at $t_s \sim 1.3$ fm is still larger than the experimental value. We are currently performing a high-statistics analysis for our physical ensemble using larger values of t_s to investigate contamination due to excited states, which tend to decrease the value of $\langle x\rangle_{u-d}$. For larger pion masses, we show results using $N_f = 2+1$ DWF from the RBC-UKQCD collaborations [74], from LHPC [67] using DWF on an $N_f = 2+1$ staggered sea, and from the QCDSF Collaboration using $N_f = 2$ clover fermions [75]. Results from LHPC used perturbative renormalization which could explain the fact that these are in general lower

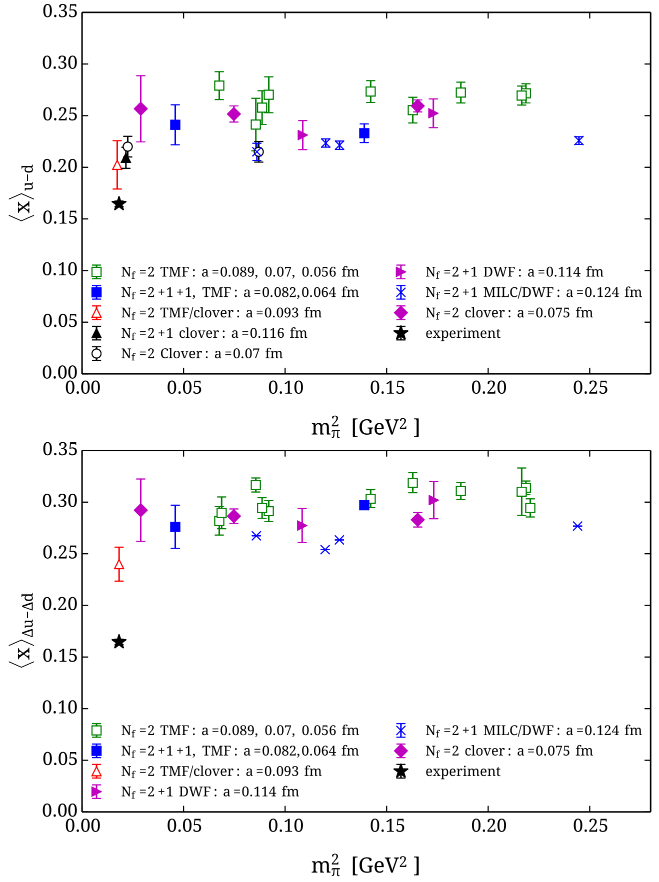

FIG. 17 (color online). Isovector nucleon momentum fraction $\langle x\rangle_{u-d}$ and helicity $\langle x\rangle_{\Delta u-\Delta d}$. Twisted mass fermion results are shown for $N_f = 2$ ensembles (open green squares), for two $N_f = 2+1+1$ ensembles (blue filled square), and for the physical ensemble with a clover term (open red triangle) taken from Table VI. Also shown are results from RBC-UKQCD using $N_f = 2+1$ DWF (magenta right pointing triangle) [74], from LHPC using DWF on $N_f = 2+1$ staggered sea (blue crosses) [67], and QCDSF/UKQCD using $N_f = 2$ clover fermions (filled magenta diamond) [75]. For $\langle x\rangle_{u-d}$, we also show results from LHPC using an $N_f = 2+1$ clover with 2-HEX smearing (filled black triangles) [66] and an $N_f = 2$ clover (open black circle) [72]. All values are extracted using the plateau method and $t_s \sim (1-1.2)$ fm, except our result at the physical point for which $t_s \sim 1.3$ fm was used. The experimental value for $\langle x\rangle_{u-d}$ is taken from Ref. [76] and for $\langle x\rangle_{\Delta u-\Delta d}$ from Ref. [77].

than other lattice results. For the case of $\langle x\rangle_{\Delta u-\Delta d}$, the situation is similar, and our value using the physical ensemble is still larger than its experimental value. As for the momentum fraction, there is a decreasing trend as t_s increases. In fact, the summation method yields a value that is consistent with the experimental value as can be seen in Fig. 11. However, the error is too large, and our goal in a future analysis is to reduce it by a factor of 2 so as to confirm agreement with the experimental value. Resolving these discrepancies will give more confidence on our prediction for the transversity moment.

VI. CONCLUSIONS

In this work, we present results on the pion momentum fraction and key nucleon observables using lattice QCD simulations at the physical value of the up- and down-quarks. Our analysis of the isovector pion momentum fraction uses $N_f = 2$ ensembles with the clover term simulated at three different values of the light quark mass. We find a value of $\langle x\rangle^{\pi^\pm}_{u-d} = 0.214(15)(^{+12}_{-9})$ in the $\overline{\mathrm{MS}}$ at 2 GeV at the physical point.

For the nucleon system, we compute the three local and three one-derivative isovector and isoscalar matrix elements at zero momentum transfer. In our calculation, we analyze three sink-source time separations, which allows us to investigate excited-state effects by observing the dependence of the extracted nucleon matrix elements on this separation. For all observables, we compare the plateau method with the summation method. In some cases, the sensitivity on the sink time t_s is good enough so that a two-state fit can also be applied as a third method to detect excited-state contaminations. Employing these different methods to ensure that contamination from excited states is suppressed is crucial in obtaining reliable results. However, for this study to be meaningful, one needs large statistics in particular for large sink-source time separations and for the summation method. For the pion momentum fraction where statistical errors are smaller, one extracts the relevant matrix element using the largest possible time separation ensuring ground-state dominance. Our results for the nucleon axial charge and isovector pion momentum fraction are in agreement with their experimental values, that constitutes a very important conclusion of this study. Since the tensor charge is found to behave similarly to the axial charge as far as ground state dominance is concerned, we can predict its value at the physical point to be $g_T^{u-d} = 1.027(62)$ in the $\overline{\mathrm{MS}}$ scheme at 2 GeV. Assuming that disconnected contributions remain as small at the physical point as were found at a pion mass of 373 MeV where they were shown to be negligible [27,28], we can give a direct prediction for the individual up- and down-quark tensor charges. We find $g_T^u = 0.791(53)$ and $g_T^d = -0.236(33)$ (see Table VI).

Thus, this first lattice study of nucleon and pion structure at the physical values of the light quark masses is very promising for future precision calculations of these key quantities directly at the physical point. Ongoing plans include an analysis with increased statistics for general momentum transfer and new $N_f = 2+1+1$ simulations with their mass fixed to physical values, combined with larger volumes and improved algorithms for noise reduction such as multiple right-hand-side solvers. After reproduction of benchmark quantities such as g_A for the nucleon and the pion, lattice QCD is in a position to turn to quantities more difficult to obtain experimentally such as the scalar and tensor charges g_S and g_T. Such charges are of high interest in phenomenology and experiments since these enter in couplings of protons to supersymmetric candidate particles.

Their precise determination can therefore be used to exclude regions in dark matter searches and influence future experimental setups for new physics searches.

ACKNOWLEDGMENTS

We would like to thank the members of the ETMC for a most enjoyable collaboration. This work was supported by a grant from the Swiss National Supercomputing Centre under Project No. s540 and in addition used computational resources from the John von Neumann-Institute for Computing on the Juropa system and the BlueGene/Q system Juqueen at the research center in Jülich and Cy-Tera at the Cyprus Institute. We also acknowledge PRACE for awarding us access to the Tier-0 computing resources Curie, Fermi, and SuperMUC based in CEA, France; Cineca, Italy; and LRZ, Germany. We thank the staff members at all sites for their kind and sustained support. This work is supported in part by the DFG Sino-German Collaborative Research Centre CRC 110 and Sonderforschungsbereich/Transregio SFB/TR9 and by funding received from the Cyprus Research Promotion Foundation under Contracts No. NEA ΥΠΟΔΟΜΗ/ΣΤΡΑΤΗ/0308/31 cofinanced by the European Regional Development Fund and No. TECHNOLOGY/ΘΕΠΙΣ/0308(BE)/17. K. H. and Ch. K. acknowledge support from the Cyprus Research Promotion Foundation under Contract No. ΤΠΕ/ΠΛΗΡΟ/0311(BIE)/09. B. K. gratefully acknowledges full financial support under AFR Ph.D. Grant No. 2773315 of the National Research Fund, Luxembourg.

APPENDIX: UPDATE OF RESULTS FROM $N_f = 2$ AND $N_f = 2+1+1$ TMF ENSEMBLES WITH PION MASSES LARGER THAN PHYSICAL

In this Appendix, we give the ETMC results for the $N_f = 2$ and the $N_f = 2+1+1$ ensembles published in Refs. [22,26], respectively. These results are updated using the new renormalization functions given in Table III. In Tables VIII and IX, we collect the results

TABLE VIII. Updated results for the $N_f = 2+1+1$ B55.32 ensemble for the nucleon charges and first moments of parton distribution functions. For the isoscalar combination, we give only the connected contribution.

	Plateau method					Summation	Two-state
t_s/a:	10	12	14	16	18	method	fit
				g_S			
Isovector	1.08(3)	1.12(3)	1.16(4)	1.08(10)	1.46(20)	1.19(10)	1.23(10)
Isoscalar	5.07(4)	5.45(4)	5.74(6)	5.95(13)	6.33(28)	6.46(15)	6.81(23)
Stat.	2429	4396	4396	2018	1200		
				g_A			
Isovector	1.143(4)	1.152(5)	1.155(8)	1.174(20)		1.184(19)	
Isoscalar	0.596(3)	0.591(4)	0.589(7)	0.605(16)		0.583(16)	
Stat.	2429	4396	4396	2018			
				g_T			
Isovector	1.119(6)	1.087(7)	1.058(11)	1.080(30)		1.023(27)	1.053(21)
Isoscalar	0.680(5)	0.666(6)	0.660(9)	0.663(21)		0.624(22)	0.646(9)
Stat.	2278	4040	4040	1762			

TABLE IX. Updated results for the $N_f = 2+1+1$ B55.32 ensemble for the nucleon first moments of parton distributions. For the isoscalar combination, we give only the connected contribution.

	Plateau method					Summation	Two-state
t_s/a:	10	12	14	16	18	method	fit
				$\langle x \rangle_q$			
Isovector	0.290(4)	0.270(3)	0.252(4)	0.233(9)	0.252(19)	0.223(9)	0.214(13)
Isoscalar	0.720(8)	0.677(5)	0.639(6)	0.607(11)	0.616(21)	0.554(15)	0.558(19)
Stat.	2429	4396	4396	2018	1200		
				$\langle x \rangle_{\Delta q}$			
Isovector	0.328(3)	0.312(3)	0.297(3)	0.298(8)		0.270(8)	0.286(9)
Isoscalar	0.207(3)	0.198(2)	0.189(3)	0.193(8)		0.172(7)	0.184(7)
Stat.	2429	4396	4396	2018			
				$\langle x \rangle_{\delta q}$			
Isovector	0.372(5)	0.349(4)	0.322(5)	0.316(12)		0.283(14)	0.284(17)
Isoscalar	0.254(4)	0.239(4)	0.219(6)	0.215(15)		0.178(14)	0.183(21)
Stat.	2278	4041	4041	1763			

for the B55.32 ensemble for which a high-statistics analysis is carried out for several sink-source separations. In Figs. 18 and 19, we show the ratios from which the isovector and isoscalar connected charges and first moments of PDFs are extracted. The ratios are computed for a total of five sink-source time separations spanning a time range of about 0.8 to 1.5 fm enabling us to apply the summation method as check for excited states. This high-statistics analysis allows us to perform a two-state fit for all quantities except the axial charge where the excited-state contamination is the mildest. As our final values, we take the plateau value that is in agreement with the value extracted from the summation method and two-state fit when possible. Finally, in Tables X and XI, we give the results for all our other ensembles where only one sink-source separation was employed.

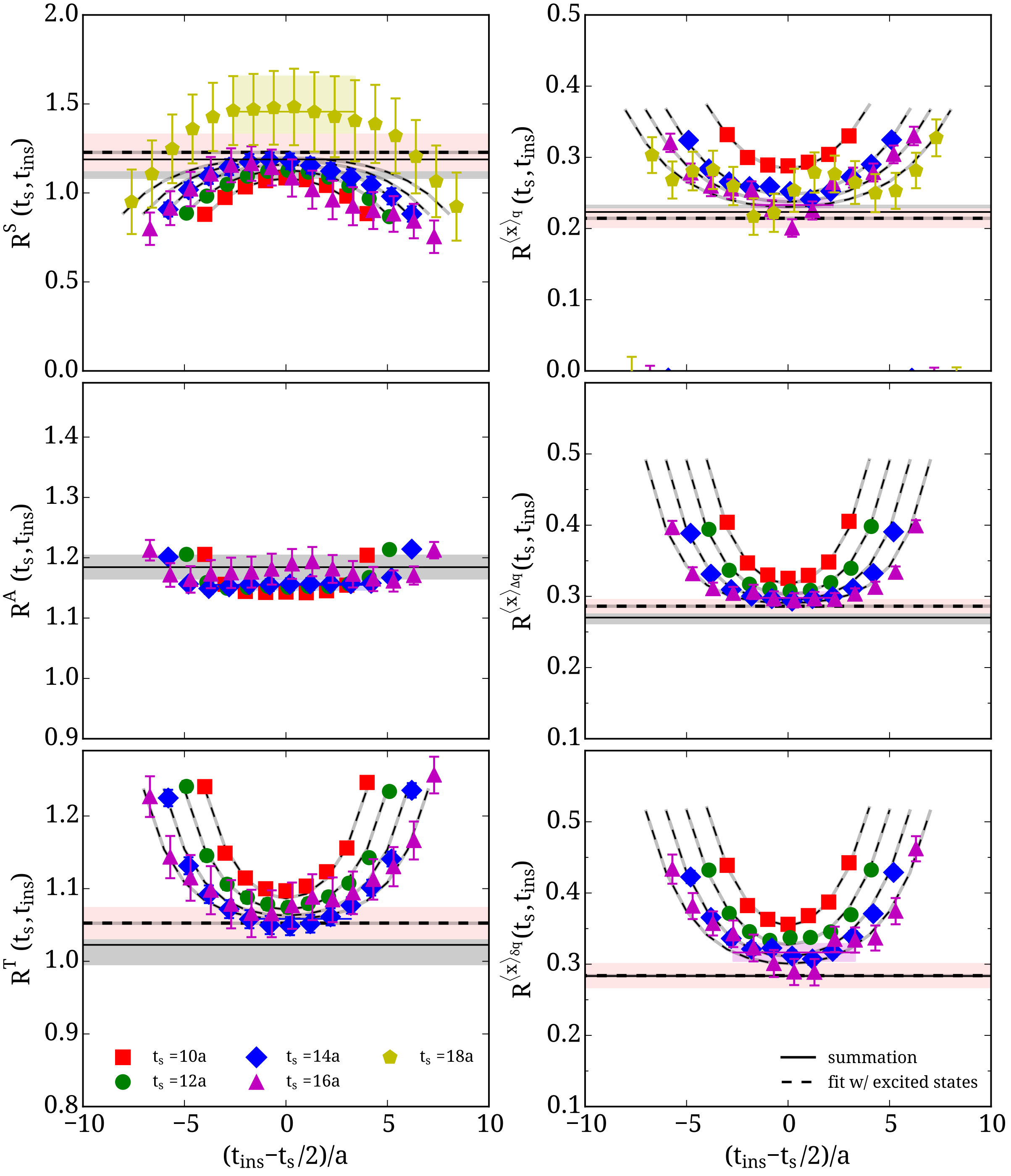

FIG. 18 (color online). The ratios from which the isovector charges (left) and the first moments of PDFs (right) are extracted as a function of the insertion-source time separation for the B55.32 ensemble. The statistics used are given in Tables VIII and IX.

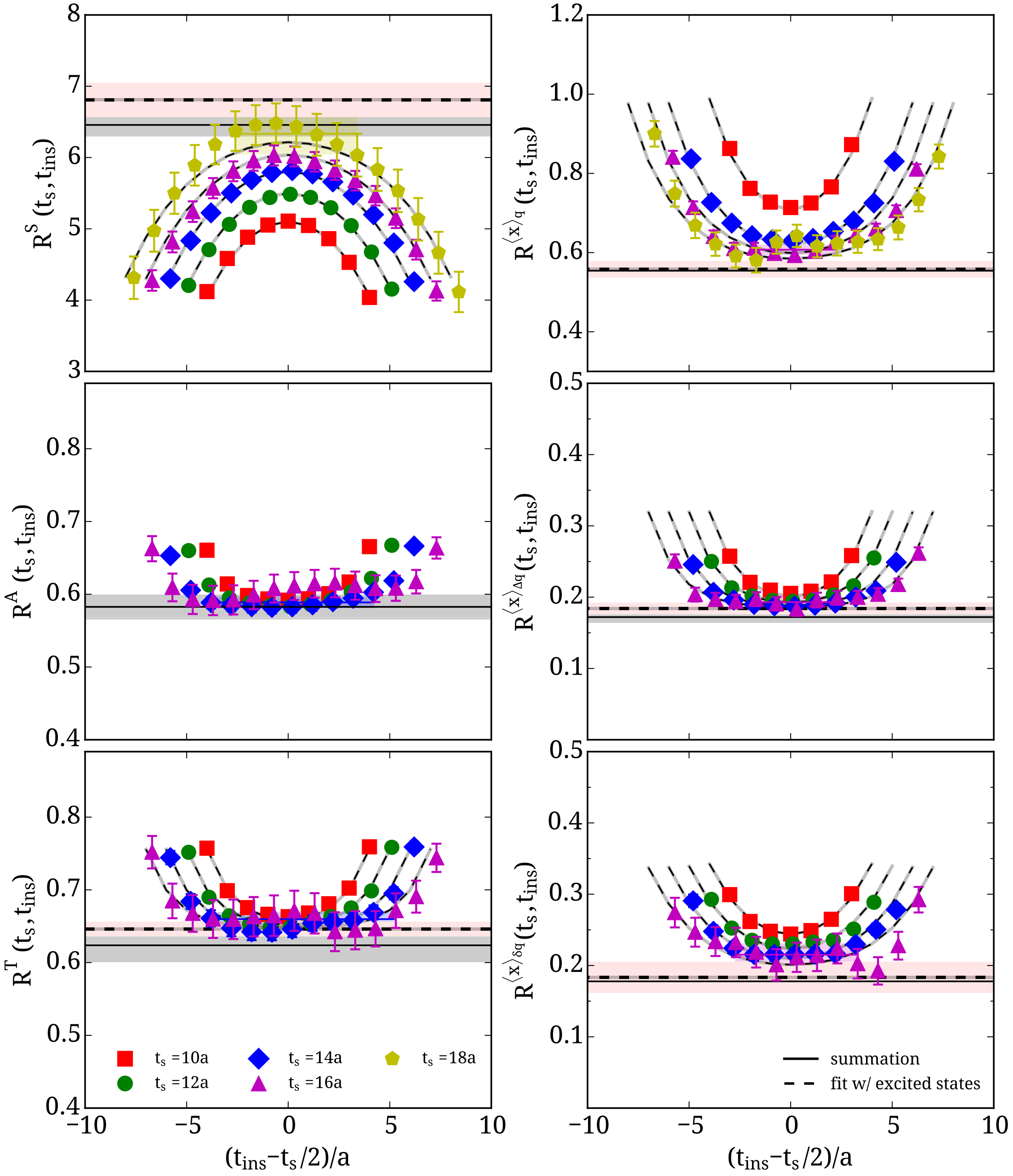

FIG. 19 (color online). The ratios from which the isoscalar charges (left) and the first moments (right) are extracted as a function of the insertion-source time separation for the B55.32 ensemble. Only connected contributions are included. The statistics used are given in Tables VIII and IX.

TABLE X. Updated results for the $N_f = 2 + 1 + 1$ TMF ensemble with $m_\pi = 213$ MeV and $a = 0.064$ fm. In the last column, we give the number of measurements for all observables.

β ($L^3 \times T$)	m_π (GeV)	g_A^{u-d}	g_S^{u-d}	g_T^{u-d}	$\langle x \rangle_{u-d}$	$\langle x \rangle_{\Delta u-\Delta d}$	$\langle x \rangle_{\delta u-\delta d}$	t_s/a	Statistics
					$N_f = 2 + 1 + 1$				
2.10 ($48^3 \times 96$)	0.2134(6)	1.185(61)	1.024(368)	1.110(61)	0.241(19)	0.276(21)	0.275(26)	18	900

TABLE XI. Updated results for the $N_f = 2$ TMF ensembles.

β ($L^3 \times T$)	m_π (GeV)	g_A^{u-d}	$\langle x \rangle_{u-d}$	$\langle x \rangle_{\Delta u-\Delta d}$	t_s/a	Statistics
			$N_f = 2$			
3.90 ($24^3 \times 48$)	0.3032(16)	1.129(34)	0.270(17)	0.291(10)	12	943
	0.3770(9)	1.158(28)	0.273(11)	0.303(9)		553
	0.4319(12)	1.152(25)	0.272(10)	0.311(8)		365
	0.4675(12)	1.181(19)	0.272(9)	0.314(6)		477
3.90 ($32^3 \times 64$)	0.2600(9)	1.174(48)	0.279(13)	0.282(14)		667
	0.2978(6)	1.121(32)	0.258(16)	0.294(10)		351
4.05 ($32^3 \times 64$)	0.2925(18)	1.211(67)	0.241(25)	0.317(24)	16	447
	0.4035(18)	1.191(32)	0.255(12)	0.319(10)		326
	0.4653(15)	1.189(25)	0.269(9)	0.310(7)		419
4.20 ($32^3 \times 64$)	0.4698(18)	1.138(25)	0.250(13)	0.294(9)	18	357
4.20 ($48^3 \times 96$)	0.2622(11)	1.142(44)	0.274(20)	0.290(15)		245

[1] V. Bernard, N. Kaiser, and U.-G. Meissner, Int. J. Mod. Phys. E **04**, 193 (1995).
[2] T. R. Hemmert, M. Procura, and W. Weise, Phys. Rev. D **68**, 075009 (2003).
[3] C. Alexandrou, *Proc. Sci.*, LATTICE2010 (2010) 001.
[4] M. Constantinou, *Proc. Sci.*, LATTICE2014 (2014) 001.
[5] C. Alexandrou *et al.*, Nuovo Cimento C **036**, 111 (2013).
[6] C. Alexandrou, Eur. Phys. J. Web Conf. **73**, 01013 (2014).
[7] S. Syritsyn, *Proc. Sci.*, LATTICE2013 (2014) 009.
[8] G. Bali *et al.*, *Proc. Sci.*, LATTICE2013 (2014) 447.
[9] R. Horsley, Y. Nakamura, A. Nobile, P. E. L. Rakow, G. Schierholz, and J. M. Zanotti, Phys. Lett. B **732**, 41 (2014).
[10] T. Bhattacharya, V. Cirigliano, S. D. Cohen, A. Filipuzzi, M. González-Alonso, M. L. Graesser, R. Gupta, and H.-W. Lin, Phys. Rev. D **85**, 054512 (2012).
[11] H. Gao *et al.*, Eur. Phys. J. Plus **126**, 2 (2011).
[12] J. Ellis and K. A. Olive, arXiv:1001.3651.
[13] G. Servant and T. M. Tait, New J. Phys. **4**, 99 (2002).
[14] G. Bertone, K. Kong, R. R. de Austri, and R. Trotta, Phys. Rev. D **83**, 036008 (2011).
[15] J. C. Collins, D. E. Soper, and G. F. Sterman, Nucl. Phys. **B261**, 104 (1985).
[16] R. Brock *et al.* (CTEQ Collaboration), Rev. Mod. Phys. **67**, 157 (1995).
[17] X. Ji, Phys. Rev. Lett. **110**, 262002 (2013).
[18] X. Xiong, X. Ji, J.-H. Zhang, and Y. Zhao, Phys. Rev. D **90**, 014051 (2014).
[19] H.-W. Lin, J.-W. Chen, S. D. Cohen, and X. Ji, Phys. Rev. D **91**, 054510 (2015).
[20] C. Alexandrou *et al.*, *Proc. Sci.*, LATTICE2014 (2014) 135.
[21] A. Abdel-Rehim *et al.* (ETM Collaboration), arXiv:1507.05068.
[22] C. Alexandrou, M. Brinet, J. Carbonell, M. Constantinou, P. A. Harraud, P. Guichon, K. Jansen, T. Korzec, and M. Papinutto (ETM Collaboration), Phys. Rev. D **83**, 045010 (2011).
[23] C. Alexandrou, J. Carbonell, M. Constantinou, P. A. Harraud, P. Guichon, K. Jansen, C. Kallidonis, T. Korzec, and M. Papinutto, Phys. Rev. D **83**, 114513 (2011).
[24] C. Alexandrou, M. Brinet, J. Carbonell, M. Constantinou, P. A. Harraud, P. Guichon, K. Jansen, T. Korzec, and M. Papinutto, Phys. Rev. D **83**, 094502 (2011).
[25] S. Dinter, C. Alexandrou, M. Constantinou, V. Drach, K. Jansen, and D. B. Renner, Phys. Lett. B **704**, 89 (2011).
[26] C. Alexandrou, M. Constantinou, S. Dinter, V. Drach, K. Jansen, C. Kallidonis, and G. Koutsou, Phys. Rev. D **88**, 014509 (2013).
[27] A. Abdel-Rehim, C. Alexandrou, M. Constantinou, V. Drach, K. Hadjiyiannakou, K. Jansen, G. Koutsou, and A. Vaquero, Phys. Rev. D **89**, 034501 (2014).

[28] C. Alexandrou, M. Constantinou, V. Drach, K. Hadjiyiannakou, K. Jansen, G. Koutsou, A. Strelchenko, and A. Vaquero, Comput. Phys. Commun. **185**, 1370 (2014).

[29] C. Alexandrou, S. Gusken, F. Jegerlehner, K. Schilling, and R. Sommer, Nucl. Phys. **B414**, 815 (1994).

[30] S. Gusken, U. Löw, K.-H. Mütter, R. Sommer, A. Patel, and K. Schilling, Phys. Lett. **B227**, 266 (1989).

[31] C. Alexandrou *et al.* (ETM Collaboration), Phys. Rev. D **78**, 014509 (2008).

[32] D. Dolgov *et al.* (LHPC Collaboration, TXL Collaboration), Phys. Rev. D **66**, 034506 (2002).

[33] S.-J. Dong and K.-F. Liu, Phys. Lett. B **328**, 130 (1994).

[34] M. Foster and C. Michael (UKQCD Collaboration), Phys. Rev. D **59**, 074503 (1999).

[35] C. McNeile and C. Michael (UKQCD Collaboration), Phys. Rev. D **73**, 074506 (2006).

[36] R. Baron *et al.* (ETM Collaboration), Proc. Sci., LAT2007 (**2007**) 153.

[37] G. Martinelli and C. T. Sachrajda, Phys. Lett. B **196**, 184 (1987).

[38] C. McNeile and C. Michael (UKQCD Collaboration), Phys. Lett. B **491**, 123 (2000).

[39] L. Maiani, G. Martinelli, M. Paciello, and B. Taglienti, Nucl. Phys. **B293**, 420 (1987).

[40] S. Capitani, M. D. Morte, G. von Hippel, B. Jäger, A. Jüttner, B. Knippschild, H. B. Meyer, and H. Wittig, Phys. Rev. D **86**, 074502 (2012).

[41] R. Frezzotti, P. A. Grassi, S. Sint, and P. Weisz (ALPHA Collaboration), J. High Energy Phys. 08 (2001) 058.

[42] R. Frezzotti and G. C. Rossi, J. High Energy Phys. 08 (2004) 007.

[43] K. Jansen, C. McNeile, C. Michael, K. Nagai, M. Papinutto, J. Pickavance, A. Shindler, C. Urbach, and I. Wetzorke, Phys. Lett. B **624**, 334 (2005).

[44] F. Farchioni, R. Frezzotti, K. Jansen, I. Montvay, G. C. Rossi, E. Scholz, A. Shindler, N. Ukita, C. Urbach, and I. Wetzorke, Eur. Phys. J. C **39**, 421 (2005).

[45] F. Farchioni *et al.*, Eur. Phys. J. C **47**, 453 (2006).

[46] P. Boucaud *et al.* (ETM Collaboration), Phys. Lett. B **650**, 304 (2007).

[47] P. Boucaud *et al.* (ETM Collaboration), Comput. Phys. Commun. **179**, 695 (2008).

[48] R. Baron *et al.* (ETM Collaboration), J. High Energy Phys. 08 (2010) 097.

[49] R. Baron *et al.*, J. High Energy Phys. 06 (2010) 111.

[50] A. Abdel-Rehim *et al.*, *Proc. Sci.*, LATTICE2013 (2013) 264.

[51] A. Abdel-Rehim *et al.*, *Proc. Sci.*, LATTICE2014 (2014) 119.

[52] C. Alexandrou, J. Carbonell, D. Christaras, V. Drach, M. Gravina, and M. Papinutto, Phys. Rev. D **86**, 114501 (2012).

[53] C. Alexandrou, V. Drach, K. Jansen, C. Kallidonis, and G. Koutsou, Phys. Rev. D **90**, 074501 (2014).

[54] J. Gasser, M. Sainio, and A. Svarc, Nucl. Phys. **B307**, 779 (1988).

[55] N. Carrasco *et al.* (European Twisted Mass Collaboration), Nucl. Phys. **B887**, 19 (2014).

[56] R. Sommer, Nucl. Phys. **B411**, 839 (1994).

[57] C. Alexandrou *et al.*, *Proc. Sci.*, LATTICE2014 (2014) 151.

[58] C. Alexandrou, M. Constantinou, K. Jansen, G. Koutsou, and H. Panagopoulos, *Proc. Sci.*, LATTICE2013 (2014) 294.

[59] M. Göckeler, R. Horsley, H. Oelrich, H. Perlt, D. Petters, P. E. L. Rakow, A. Schäfer, G. Schierholz, and A. Schiller, Nucl. Phys. **B544**, 699 (1999).

[60] M. Constantinou, V. Lubicz, H. Panagopoulos, and F. Stylianou, J. High Energy Phys. 10 (2009) 064.

[61] C. Alexandrou, M. Constantinou, T. Korzec, H. Panagopoulos, and F. Stylianou, Phys. Rev. D **83**, 014503 (2011).

[62] C. Alexandrou, M. Constantinou, and H. Panagopoulos (ETM Collaboration), arXiv:1509.00213.

[63] M. Constantinou *et al.* (ETM Collaboration), J. High Energy Phys. 08 (2010) 068.

[64] K. Wijesooriya, P. Reimer, and R. Holt, Phys. Rev. C **72**, 065203 (2005).

[65] G. S. Bali S. Collins, B. Gläßle, M. Göckeler, J. Najjar, R. H. Rödl, A. Schäfer, R. W. Schiel, W. Söldner, and A. Sternbeck, Phys. Rev. D **91**, 054501 (2015).

[66] J. Green, M. Engelhardt, S. Krieg, J. W. Negele, A. V. Pochinsky, and S. N. Syritsyn, Phys. Lett. B **734**, 290 (2014).

[67] J. D. Bratt *et al.* (LHPC Collaboration), Phys. Rev. D **82**, 094502 (2010).

[68] T. Bhattacharya, S. D. Cohen, R. Gupta, A. Joseph, H.-W. Lin, and B. Yoon, Phys. Rev. D **89**, 094502 (2014).

[69] J. Green, J. W. Negele, A. V. Pochinsky, S. N. Syritsyn, M. Engelhardt, and S. Krieg, Phys. Rev. D **86**, 114509 (2012).

[70] T. Bhattacharya, V. Cirigliano, S. D. Cohen, R. Gupta, A. Joseph, H.-W. Lin, and B. Yoon, Phys. Rev. D **92**, 094511 (2015).

[71] R. Gupta, T. Bhattacharya, A. Joseph, S. D. Cohen, and H.-W. Lin, *Proc. Sci.*, LATTICE2013 (2014) 409.

[72] G. S. Bali, S. Collins, B. Gläßle, M. Göckeler, J. Najjar, R. H. Rödl, A. Schäfer, R. W. Schiel, A. Sternbeck, and W. Söldner, Phys. Rev. D **90**, 074510 (2014).

[73] G. S. Bali, S. Collins, M. Deka, B. Gläßle, M. Göckeler, J. Najjar, A. Nobile, D. Pleiter, A. Schäfer, and A. Sternbeck, Phys. Rev. D **86**, 054504 (2012).

[74] Y. Aoki, T. Blum, H.-W. Lin, S. Ohta, S. Sasaki, R. Tweedie, J. Zanotti, and T. Yamazaki, Phys. Rev. D **82**, 014501 (2010).

[75] D. Pleiter *et al.* (QCDSF/UKQCD Collaboration), *Proc. Sci.*, LATTICE2010 (2010) 153.

[76] S. Alekhin, J. Blumlein, and S. Moch, Phys. Rev. D **86**, 054009 (2012).

[77] J. Blumlein and H. Bottcher, Nucl. Phys. **B841**, 205 (2010).